Transcription Factor Condensates Mediate Clustering of *MET* Regulon and Enhancement in Gene Expression

James Lee [1,2], Leman Simpson [2,3], Yi Li [1,2], Samuel Becker [1], Fan Zou [4], Xin Zhang [3], and Lu Bai[1,2,4*]

[1]Department of Biochemistry and Molecular Biology, [2]Center for Eukaryotic Gene Regulation, [3]Department of Chemistry, [4]Department of Physics, The Pennsylvania State University, University Park, PA, 16802, USA

*Corresponding author: lub15@psu.edu, (814) 863-4824

Abstract

Some transcription factors (TFs) can form liquid-liquid phase separated (LLPS) condensates. However, the functions of these TF condensates in 3D genome organization and gene regulation remain elusive. In response to methionine (met) starvation, budding yeast TF Met4 and a few co-activators, including Met32, induce a set of genes involved in met biosynthesis. Here, we show that the endogenous Met4 and Met32 form co-localized puncta-like structures in yeast nuclei upon met depletion. Recombinant Met4 and Met32 form mixed droplets with LLPS properties *in vitro*. In relation to chromatin, Met4 puncta co-localize with target genes, and at least a subset of these target genes is clustered in 3D in a Met4-dependent manner. A *MET3pr*-GFP reporter inserted near several native Met4 binding sites becomes co-localized with Met4 puncta and displays enhanced transcriptional activity. A Met4 variant with a partial truncation of an intrinsically disordered region (IDR) shows less puncta formation, and this mutant selectively reduces the reporter activity near Met4 binding sites to the basal level. Overall, these results support a model where Met4 and co-activators form condensates to bring multiple target genes into a vicinity with higher local TF concentrations, which facilitates a strong response to methionine depletion.

Introduction

Chromosomes form extensive 3D contacts that can occur over long linear genomic distances (Misteli 2020). A subset of these interactions, such as promoter-promoter or promoter-enhancer looping, is thought to play a central role in gene regulation (Schoenfelder and Fraser 2019) . In some cases, multiple genes come together in 3D space to form “multi-gene clusters”, and these clusters often involve co-regulated genes responding to stress or other types of environmental cues, such as heat shock, starvation, virus infection, or developmental signals (Du and Bai 2017; Lim and Levine 2021; Uyehara and Apostolou 2023; Zhao and Faryabi 2023). Evidence from imaging and genomic studies suggests that these gene clusters may be related to a phenomenon called “transcription factories”, where RNA polymerase II (Pol II), mediator, and nascent transcripts coalesce into distinct foci (Carter et al. 2008; Sutherland and Bickmore 2009; Rieder et al. 2012). Proteomic analysis of transcription factories showed that they are also enriched with other components in the transcription pathway, including transcription factors (TFs), histone modification enzymes, and chromatin remodelers (Lyons et al. 2023). Overall, these observations suggest that some co-regulated genes can physically cluster into sub-nuclear compartments with elevated local concentrations of transcription-related factors.

How multi-gene clusters are formed is not well understood. Since co-regulated genes are often activated by a common set of TFs, such clustering may be mediated by the DNA-protein and protein-protein interactions of the TFs. Recent studies showed that TFs like Gcn4, OCT4, and TAZ, as well as some co-factors such as the mediator and histone-acetylation reader Brd4, tend to form biomolecular condensates through liquid-liquid phase separation (LLPS) (Whyte et al. 2013; Boija et al. 2018; Sabari et al. 2018; Lu et al. 2020). In LLPS, multivalent interactions among proteins, often through their intrinsically disordered regions (IDRs), allow them to condense into liquid-like droplets that are separated from the aqueous phase (Banani et al. 2017; Dignon et al. 2020). The existence of TF / co-factor condensates is supportive of the “transcription factory” model mentioned above where transcription-related factors are locally concentrated through LLPS. So far, LLPS of TFs and co-factors has often been studied *in vitro* using purified systems or *in vivo* with artificial induction. How these proteins behave in a chromatin context at the endogenous concentration, and more specifically, if they contribute to multi-gene cluster formation, is not very clear.

Another unresolved issue related to multi-gene clusters is their functional role in gene regulation. Earlier studies of gene clusters found a positive correlation between clustering and gene expression level (Apostolou and Thanos 2008; Fullwood et al. 2009; Li et al. 2012; Fanucchi et al. 2013; Zhang and Bai 2016; Mir et al. 2018; Zhu et al. 2021), but the mechanism of the phenomenon was not clear. This again may be related to TF / co-factor condensates: if a gene cluster is situated within a condensate, higher local concentrations of these factors can potentially enhance expression. This is proposed to be the case at super-enhancers, where the condensates of co-factors like Med1 and Brd4 are thought to drive the high transcriptional activities of the target genes. However, some reports studying TF condensates reveal a complex, sometimes contradictory, relation to gene expression, where the condensates are observed to have positive, negative, or neutral effects on transcription (Chong et al. 2022). In a recent study of the *GAL* genes, for example, it is proposed that Gal4 condensation facilitates their recruitment to target genes but does not contribute to gene activation (Meeussen et al. 2023). In general, the relation between TF condensates, multi-gene cluster, and gene regulation needs to be further studied.

Upon met depletion (-met) in budding yeast, Met4 is recruited by several sequence-specific DNA-binding co-activators, including Cbf1, Met31, and Met32, to bind and rapidly activate a subset of genes (Thomas et al. 1992; Lee et al. 2010; Ouni et al. 2010; Carrillo et al. 2012). This activator complex is further stabilized by Met28 (Kuras et al. 1997). In a previous study, we carried out a screen to probe long-distance gene regulation that affected *MET3* promoter (*MET3pr*) activity by inserting an insulated *MET3pr*-GFP reporter into many genomic loci and measuring GFP intensity in -met (Du et al. 2017). At most locations, the reporter has comparable induction level; however, it shows enhanced activity at a small subset of loci, which were defined as “transcriptional hotspots” (Du et al. 2017). These hotspots tend to be located near endogenous Met4 target genes, and 3C assay detects physical proximity among the hotspots. These results led to a hypothesis that hotspots occur at loci where *MET* genes cluster, and such clustering and transcriptional elevation may be both mediated by the condensates of related TFs.

In this study, we test the hypothesis above using a combination of biochemistry, genetics, genomics, and imaging approaches. We demonstrate that Met4 and Met32 form co-localized puncta in the yeast nuclei upon met depletion. Purified Met32 forms condensate with LLPS

properties *in vitro*, with which Met4 can merge. In relation to chromatin, we show that the loci that are associated with the Met TFs co-localize with the Met4 puncta, and at least a subset of Met4 target genes cluster in 3D nuclear space in a Met4-dependent manner. Functionally, the *MET3pr-GFP* reporter inserted near the endogenous Met4 target sites shows higher enrichment of Met TFs / Pol II and enhanced transcriptional activity (hotspots). A Met4 IDR truncation that reduces Met4 puncta formation selectively affects the reporter activity at hotspots. Collectively, our results support a model where TFs in the met response pathway form LLPS condensates, organize multiple target genes in their vicinity, and enhance gene expression by creating a local environment with elevated concentrations of transcription-related factors. This may represent a common strategy for cells to concentrate limited resources to mount a strong response to stress.

Results

The trans-activator Met4 and its co-factor Met32 form puncta in the nucleus. Our previous study presented evidence that the "hotspots" for *MET3pr* transcription may form 3D clusters, but the mechanisms of clustering and transcriptional elevation are unknown. Given the recent reports on TF condensation (Sabari et al. 2018; Lu et al. 2020; Zhang et al. 2022; Okada et al. 2023), we hypothesize that these phenomena may be related to condensates formed by TFs in the *MET* pathway. To test this possibility, we labeled the endogenous Met4 protein with GFP and visualized Met4 in live cells under Airyscan confocal microscopy (**Materials and Methods**; see **Table S1** for strain list). We observed nuclear-localized Met4-GFP under both the repressed (+met) and activated (-met) conditions, with the latter showing higher intensity. Importantly, the Met4-GFP displays puncta-like structures, especially under -met (**Fig. 1A & S1A**). As controls, we constructed strains expressing a nuclear-localized free GFP or GFP fused to various chromatin-associated factors, including TFs Cbf1 and Reb1, and Sth1, a subunit of RSC nucleosome remodeler, which also bind chromatin with sequence specificity (Cai and Davis 1990; Ju et al. 1990; Donovan et al. 2023). The GFP signals appear more evenly distributed in these control strains (**Fig. 1A**). To evaluate the distribution more quantitatively, we calculated the coefficient of variance (CV) of the fluorescent intensities among the pixels inside each nuclei (**Materials and Methods**, **Table S2**). Uneven distribution of the GFP molecules would result in large variations in the pixel intensities and higher CVs. The CVs of Met4-GFP in both ±met conditions are significantly higher than free GFP and other nuclear proteins (**Fig. 1B**). Since the strains in **Fig. 1A** express GFP at different levels, which directly affects CV, we also calculated the Fano number (variance divided by the mean) to control for

this variable. Met4-GFP in the -met condition has the largest Fano number (**Fig. 1C & S1B**), which indicates that in the activated state it forms the most punctate structures. This data supports the notion that Met4 forms condensates in the nuclei upon activation.

We next carried out the same experiment with Met32, the DNA binding co-factor of Met4. We imaged cells containing endogenous Met32 labeled with mCherry and compared its distribution to free mCherry. Unlike Met4, Met32-mCherry is barely visible in +met, and it is significantly upregulated in -met (**Fig. 1D & S1C**). In the latter condition, Met32-mCherry also shows uneven distribution with high CV and Fano number (**Fig. 1E, F & S1D**). We also imaged Met31-mCherry, but its concentration is too low to be detected. When Met4-GFP and Met32-mCherry are tagged in the same strain, their fluorescent signals largely overlap (**Fig. 1G & S1E**). To quantify the overlap, we extracted the GFP and mCherry fluorescence intensities for all the pixels inside each nucleus and calculated their correlation coefficient. As a control, we carried out the same analysis with co-expressed Sth1-GFP and Met32-mCherry, which appear to be less co-localized (**Fig. 1G**). Indeed, the Pearson correlation between Met4 and Met32 fluorescence on average was 0.75, much higher than that between Sth1 and Met32 (R = 0.19) (**Fig. 1H**). Overall, the puncta-like structures of Met4 and Met32 and their co-localization support the possibility that these two factors co-condense under the -met condition.

Met32 forms condensates with LLPS properties *in vitro.* LLPS is proposed to be a mechanism that leads to TF condensation (Banani et al. 2017; Boeynaems et al. 2018). To test whether this mechanism applies to Met4 and Met32, we first evaluated their propensity to phase separate using the FuzDrop algorithm (Hatos et al. 2022). All the Met activators, including Met4, Met31, Met32, and Met28, are predicted to have higher LLPS probabilities than GFP and mCherry (**Fig. 2A**). Among these TFs, Met4 and Met32 have particularly high scores, which suggests they function as droplet drivers that can spontaneously phase separate (Vendruscolo and Fuxreiter 2022). In addition, both factors are predicted to have large unstructured domains, a feature known to promote LLPS (**Fig. S2A & B**).

We next purified Met4 and Met32 to study their condensation properties *in vitro*. Like many other recombinant TFs, Met4 is prone to degradation. We managed to extract full length Met4 tagged with 6xHis and MBP on the N- and C- terminus, respectively, although some degradation products could not be avoided (**Fig. 2B**) (**Materials and Methods**). We imaged the purified

Met4 labeled with Alexa488 in various buffers. Met4 remains diffusive up to 5 μM at physiological salt concentrations and forms aggregates at higher density or lower salt concentrations (**Fig. 2C**). Although these results suggest that Met4 may not inherently undergo LLPS, we cannot rule out the potential effects from impurities (degradation products) and tags on our observations. In contrast, we managed to purify high-quality Met32 fused with mCherry (**Fig. 2B**). At the physiological salt concentration with no crowding agents, Met32-mCherry forms condensates at various concentrations from 1 to 20 μM (**Fig. 2C & S2C**). These condensates show properties consistent with LLPS such as droplet fusion (**Fig. 2D**) and fluorescent recovery after photobleaching (FRAP) (**Fig. 2E**). The Met32-mCherry condensates have a 64 ± 9.7s half recovery time, comparable to well-established LLPS proteins such as FUS (5-120 seconds), DDX4 (3-200 seconds), and hnRNPA1 (5-120 seconds) (Nott et al. 2015; Shin et al. 2017; McSwiggen et al. 2019).

To further test potential Met4 / Met32 co-condensation, we added purified Met4 and Met32 together in 150 mM NaCl buffer and imaged in both Alexa488 and mCherry channels. The two proteins are mixed into droplets in solution (**Fig. 2F**). In these co-localized droplets, Met32-mCherry still undergoes FRAP recovery with a slightly slower rate (83 ± 11s half recovery time) (**Fig. S2D**). These results are consistent with the idea that Met4 and Met32 can co-condense through a LLPS mechanism *in vitro*, which may contribute to the Met4 / Met32 puncta formation *in vivo*.

Met4-activated genes co-localize with Met4 puncta. Since Met32 is a sequence-specific DNA binder, the Met4 / Met32 condensates can potentially contact multiple target genes. This leads to our model in **Fig. 3A**, which predicts that 1) at least some Met4 activated genes should be co-localized with Met4 condensates, and 2) multiple target genes should cluster in 3D. To test these predictions, we first performed chromatin immunoprecipitation with sequencing (ChIP-seq) of related TFs (Met4, Met32, Met28, Cbf1), as well as RNA-seq, to identify genes directly targeted by Met4. As expected, the bindings of Met4, Met32, and Met28 are strongly induced by met depletion, while Cbf1, an abundant pioneer factor (Kuras et al. 1996; Blaiseau and Thomas 1998; Ouni et al. 2010; Carrillo et al. 2012; Yan et al. 2018; Donovan et al. 2019), shows constitutive binding (**Fig. 3B & C, S3A & B**). Under the induced condition, we identified 34 regions co-bound by all four TFs (**Fig. 3C, Table S3**), and these binding sites potentially regulate 46 genes (some sites are located in divergent promoters). Met depletion for 2 hrs

causes wide-spread changes in the mRNA level with both up- and down-regulation (**Fig. 3D, S3C**), reflecting the fundamental role of methionine in metabolism (Thomas and Surdin-Kerjan 1997). Importantly, 40 out of the 46 genes co-bound by all four TFs show significantly increased expression under the -met condition (**Fig. 3D, Table S4**), indicating that they are direct targets of Met4 and its co-activators.

To determine if the Met4 target genes are co-localized with the Met4 puncta, we inserted 196X tetO repeats near two of these genes, *MET13* and *MET6*, which allows us to visualize these loci through their association with tetR-mCherry. We also created control strains with the same array inserted near *PUT1* and the mating locus *MAT,* two loci with no Met4 association. These chromatin dots were imaged together with Met4-GFP under ±met conditions. Visually, *MET13* and *MET6* loci have higher probabilities to be co-localized with Met4 puncta in -met compared to *MAT* and *PUT1* (**Fig. 3E**). To test this more quantitatively, we aligned these images with the chromatin dots at the center and averaged the surrounding GFP signals (**Materials and Methods**). For all four loci, the averaged GFP intensities are higher near the center because the distant pixels are more likely to be outside nuclear boundaries, where Met4 signals are absent (**Fig. 3F & G**). In +met condition, Met4-GFP has low intensities. Upon activation, we can see localized GFP dots with heightened peak intensities at the *MET13* and *MET6* loci in comparison to controls (**Fig. 3F & G**). These results indicate that at least some Met4 target genes are associated with Met4 condensates upon activation, presumably through sequence-specific co-binders like Met32.

Met4-dependent clustering of *MET* genes upon induction. We next tested the second prediction of the model in **Fig. 3A**, i.e., Met4 condensates mediate the 3D clustering of target genes. We first carried out a Hi-C measurement under -met condition, which did not show any significant interactions among Met4 targets (Li et al. 2024). Given the limitations of Hi-C in detecting fine-scale interactions (Oluwadare et al. 2019), we used an assay recently developed in our lab, Methyltransferase Targeting-based chromosome Architecture Capture (MTAC) (Li et al. 2024), to identify potential chromosomal interactions with selected Met4 targets (**Materials and Methods**). In this method, a 256X LacO array is inserted near the gene of interest (viewpoint, or VP) to recruit LacI fused with DNA methyltransferase M.CviPI, which methylates proximal cytosines in the “GC” context in *cis* and in *trans* (**Fig. 4A**). Physical proximity to the VP

can thus be evaluated based on the enrichment of the methylation signal in comparison to a control strain containing the same LacI-M.CviPI but no LacO array.

In a previous study (Li et al. 2024), we performed MTAC assays with a VP near the *MET6* gene under ± met condition. This VP 3kb away from *MET6* captures highly specific inter-chromosomal interactions with four other Met4-targeted genes under -met, but not +met, condition (Li et al. 2024). To further illustrate this point, we carried out MTAC with *MET13* as the VP (**Fig. 4B**). Under +met condition, MTAC only detects interactions from the adjacent local chromatin (**Fig. 4C, S4A**). When the same strain was switched to the -met condition, MTAC captures two far-*cis* interactions (intra-chromosomal interactions that are over 30kb apart) with two promoter regions near Met4 targeted genes (*STR3*, *MUP1*) (**Fig. 4C, S4A**). Interestingly, these two regions were also found to interact with the *MET6* VP . Taken together, these data support the clustering of a subset of Met4-targeted genes upon activation.

The model in **Fig. 3A** implies that the clustering of *MET* genes is mediated by Met4 / Met32. To test this idea, we carried out MTAC using the *MET6* VP ± acute auxin-induced degradation of Met4 ± met (**Fig. S4B & C**). For the -met experiment, auxin (IAA) was added 30 mins prior to the met depletion so that Met4 activation would be largely eliminated (**Fig. 4D**). This would also prevent the accumulation of Met32, as it relies on Met4 for induction (Menant et al. 2006; Lee et al. 2010; Carrillo et al. 2012). Consistent with our previous observations, very few long-distance interactions were found in the +met repressed condition, regardless of the presence or absence of Met4 (**Fig. 4E & F, (1) and (3)**). Upon met depletion without IAA addition, we observed significant *trans* (inter-chromosomal) interactions between the *MET6* locus with three other Met4-targeted genes (*MUP1*, *STR3*, *YKG9*) (**Fig. 4E & F, (2)**). Importantly, these interactions disappear when Met4 was degraded (**Fig. 4E & F, (4)**). These data show that the presence of Met4, and likely Met32, is required for *MET* gene clustering. This is consistent with the model in **Fig. 3A** that clustering is mediated by Met4 / Met32 condensates.

Regions near Met TF binding sites constitute *MET* "transcriptional hotspot" in haploid yeast. We next investigated the functional role of Met4 condensates in gene expression. In our previous screen, we identified the *MET13* locus on chr7 as a "transcriptional hotspot": when the *S.kud MET3pr*-GFP reporter was inserted into *MET13* or neighboring genes, it showed higher GFP expression than most of the other insertion sites upon induction (Du et al. 2017).

Combined with the observation that *MET13* locus co-localizes with the Met4 puncta (**Fig. 3E-G**), this suggests a potential link between the higher reporter activity and Met4 / Met32 condensates. However, the initial screen was performed in diploids, while all the experiments above were carried out in haploids. We therefore first tested if *MET13* also functions as a transcriptional hotspot in haploid yeast. We again used the *S.kud MET3pr* for this test, as the sequence of this promoter deviates significantly with the endogenous *MET3pr*, allowing them to be differentiated in PCR (Du et al. 2017).

We created two haploid strains with the *S.kud MET3pr*-GFP reporter inserted near the *MET13* gene (*CWC23* and *RSM23*) and measured its transcriptional profile (**Fig. 5A**) (**Materials and Methods**). For comparison, we also inserted the same reporter into two basal loci *ATG36* and *LDS2* (**Fig. 5A**). *ATG36* and *LDS2* loci are not associated with Met4 and its co-factors, and these two genes are not induced by -met. The GFP intensities from the reporter at *CWC23* and *RSM23* loci are ~50% higher (*P*-value < 1e-4) compared to the control under the -met condition (**Fig. 5B**). Reporter GFP mRNA levels, as well as Pol II associated with the GFP ORF, are also significantly higher in the former strains (**Fig. 5C & D**). These results are consistent with our previous observations in diploid cells that the *MET13* locus promotes the transcriptional activity of the *MET3pr*.

Given the model in **Fig. 3A**, we reasoned that the enhanced activities of the GFP reporter may be due to increased local concentrations of TFs, which likely lead to higher TF occupancies. To test this idea, we performed ChIP of Met4 and Met32 followed by qPCR on the *S.kud MET3pr* at the hotspot vs basal genomic locations because it contains a Met32 motif. Consistent with our expectation, we observed higher enrichment of Met4 and Met32 over the *S.kud MET3pr* at hotspot locations (**Fig. 5E & F**). Taken together, these findings confirm the existence of "hotspot" loci in haploid yeast and suggest that it may be caused by enhanced binding of Met32 and Met4.

Reporter activities near Met4 binding sites are enhanced over a ~40kb range. Besides *MET13*, other loci that colocalize with Met4 puncta, like *MET6* (**Fig. 3E-F**), should also function as transcriptional hotspots. To test this idea, we first verified that *MET6* remains associated with Met4 puncta after the reporter insertion. We used the *MET6* yeast strain in **Fig. 3E** and integrated a *S.kud MET3pr* reporter nearby (**Fig. 6A**). This reporter contains a frame-shifted

GFP (fsGFP) in order not to interfere with the Met4-GFP signal. As controls we integrated the same reporter near two genomic regions not bound by Met TFs (*PUT1* and *ATG36*). We imaged these strains in -met and analyzed them with the same method used in **Fig. 3F**. Interestingly, despite the fact that *S.kud MET3pr* is bound and activated by Met4, insertion of this promoter does not increase the local Met4 intensity at *MET6* and *PUT1* (**Fig. 6B & C**, ± rep). In comparison with the reporter-containing *PUT1* and *ATG36* loci, *MET6* again shows stronger co-localization with the Met4 puncta (**Fig. 6B & C**). This finding indicates that *S.kud MET3pr* alone is insufficient in nucleating a new Met4 condensate or recruiting the integrated locus to an existing condensate.

We then integrated the original *S.kud MET3pr*-GFP reporter into *MET6*, *ATG36*, and *LDS2* (the latter two are controls far from any endogenous Met4 binding sites) (**Fig. 6D**) and compared their GFP expressions. GFP shows significantly higher intensity at *MET6* in comparison with the two basal loci (*P*-value < 1e-4) (**Fig. 6E**). To test the generality of this observation, we inserted the reporter into two additional genomic loci associated with Met TFs, *MET17* and *RMD6*, and the reporter shows higher GFP expression in both loci (**Fig. 6E**). This data supports a model where Met4 condensates associated with the endogenous *MET* genes enhance the activity of a nearby reporter. This model also predicts that such enhancement effect should be specific to the met pathway, i.e., inducible genes activated by other TFs should not benefit from higher local concentrations of *MET* activators. We tested this idea by inserting into the same loci a GFP reporter driven by either *MET17pr*, a promoter in the same pathway, or by *GAL1Spr*, an attenuated *GAL1* promoter controlled by a different set of TFs in another pathway (Mumberg et al. 1994). Indeed, *MET17pr* shows the same trend as *MET3pr*, while the strengths of *GAL1Spr* remain constant across all these loci (**Fig. 6F**). These results demonstrate the pathway-specificity of the transcriptional hotspots.

We next conducted experiments to determine the genetic range of the transcriptional hotspot. We inserted the GFP reporter driven by *MET3pr* or *GAL1Spr* at various distances from the Met4 binding site in the *MET6* promoter (**Fig. 6G**). *MET3pr*-GFP shows higher expression level when inserted up to 30kb upstream and 10kb downstream of the Met4 site. Beyond this region, the *MET3pr* activity returns to the basal level (**Fig. 6H**). In contrast, *GAL1Spr* shows similar activities among these insertion sites (**Fig. 6H**). These data indicate that, at least near the *MET6* gene, the elevated expression of the *MET3pr* can occur over a ~40kb region.

The deletion of a disordered region in Met4 reduces puncta formation and reporter expression at transcriptional hotspots. To determine the relation between Met4 condensates and its gene regulatory function more directly, we introduced mutations to Met4 to reduce its propensity to form condensates. Since LLPS is often promoted by IDRs, we first performed PONDR analysis of Met4 (Xue et al. 2010). This analysis reveals three distinct stretches of IDRs interspersed with two previously annotated functional domains: the activation domain (aa95-144), which interacts with mediator, and the auxiliary domain (aa312-375), which interacts with Met31/32 (**Fig. 7A**) (Kuras and Thomas 1995). AlphaFold also predicts that Met4 is largely devoid of folded structures (**Fig. S2A**) (Jumper et al. 2021). To probe the effect of these IDRs on Met4 puncta formation, we first truncated individual IDR stretches: ΔIDR1 (aa1-69), ΔIDR2 (aa117-359), or ΔIDR3 (aa397-651). As Met4 is essential for cell viability in the -met media, we constructed strains containing the endogenous unlabeled Met4 with an additional copy of truncated Met4-GFP driven by the native *MET4* promoter. This allows us to visualize Met4 mutants without hindering cell growth (**Fig. 7B**). Deletions of IDR2 and IDR3 both lead to significant reductions in Met4-GFP Fano number, with ΔIDR2 having a slightly more pronounced effect (**Fig. 7B & C, S5A**). Purified Met4-ΔIDR2 show less partitioning into the Met32 condensates (**Fig. S5B**), which may contribute to the decreased puncta formation. To further specify the part of IDR2 that affects Met4 condensates, we generated shorter truncations within IDR2, ΔIDR2.1 (aa117-135), ΔIDR2.2 (aa136-270), and ΔIDR2.3 (aa271-359). All three truncations result in intermediate GFP Fano number between the full length Met4 and Met4-ΔIDR2 (**Fig. 7C, S5C & D**). These findings suggest that multiple IDRs contribute to Met4 condensation, and deleting parts of the Met4 IDR can diminish, but not completely eliminate, Met4 puncta formation.

When the full length Met4 is replaced by Met4 ΔIDR2.3, the strain is viable in the absence of met, allowing us to evaluate the functional consequence of this mutant on Met4 binding and transcriptional activation. Given our model and supporting evidence that Met4 condensates increase local TF concentration at Met4 targeted genes and enhance their expression, we expect a Met4 mutant less prone to condense will result in diminished Met4 binding and reduced induction. We therefore compared the ChIP-seq and RNA-seq data of the full-length vs truncated Met4. Consistent with the idea above, the Met4 ΔIDR2.3 shows decreased binding across all the previously annotated Met TF binding sites, without generating new ChIP-seq

peaks (**Fig. 7D & E**). Interestingly, the three Met4 binding sites near *MUP1*, *STR3*, and *YKG9* that cluster with *MET6* show significantly more reduction in Met4 ChIP-seq peaks (reduced to 42±4%) than other Met4 sites (61±8%, *P*-value = 0.02) in the Met4 ΔIDR2.3 strain. Out of the 40 potential target genes, 22 show significant decreases in their mRNA level (**Fig. 7F, S5E, Table S4**). Importantly, our model also predicts that decreased Met4 condensation should have more impact on target genes that are located near Met4 puncta than those farther away. To test this idea, we again took advantage of the *MET3pr*-GFP reporter inserted into hotspots and basal loci. We expect the reduced Met4 condensation to have a larger impact on the reporter activity in the former case because the reporter is only associated with Met4 puncta at hotspots (**Fig. 6B**). Indeed, after substituting Met4 with Met4-ΔIDR2.3 in these strains, we observed strong decreases in the reporter gene activity in hotspots but minimal effect on those in basal regions (**Fig. 7G**). These findings collectively support a model wherein Met4 condensates cluster target genes, enhance their activity, and give rise to the formation of transcriptional hotspots.

Discussion

In this study, we investigated TF distribution, 3D genome organization, and gene activation in the met response pathway using a combination of genetics, genomics, and imaging approaches. Our findings connect three emerging phenomena in gene regulation: TF condensates, co-regulated gene clusters, and transcriptional hotspots. More specifically, we show that the activator Met4 and its co-factor Met32 form puncta-like structures that co-localize with at least some Met4 target genes. Multiple *MET* genes on different chromosomes cluster in the 3D nuclei space, and such clustering requires the presence of Met4. Chromosomal loci near endogenous Met4 binding sites, in one case within a 40kb range, are hotspots for *MET3pr* reporter expression. Mutations that decrease Met4 puncta formation lead to selective reduction of the reporter transcriptional activity at the hotspots.

Condensate formation of Met4 and Met32. Using live-cell imaging, we found that fluorescently labeled Met4 and Met32 from puncta-like structures in yeast nuclei under the -met condition. This is reflected by the higher Fano numbers in Met4 / Met32 pixel intensities in comparison to free GFP, and in the case of Met4, other chromatin-associated factors. Although Met4 can form smaller puncta in the +met condition (**Fig 1A**), it cannot be recruited to its target genes due to the absence of its sequence-specific binding partners and therefore does not have 3D genome organization and gene regulatory functions. High-resolution microscopy of yeast TFs is

challenging due to the small size of the nuclei. The low intensities of the Met4 / Met32 signals require high excitation for imaging, which also makes them prone to photobleaching. Thus, we were unable to measure Met4 and Met32 puncta dynamics *in vivo*. When purified *in vitro*, Met32-mCherry readily forms droplets with typical LLPS properties without molecular crowder, while His- and MBP-tagged Met4 remain diffusive at physiological salt concentration. We also found that Met4 partitions into the Met32 droplets when they are mixed, and inside cells, the two factors show significant co-localization. These observations raise the intriguing possibility that Met32 serves as a scaffold to nucleate the co-condensates of Met4 and other Met TFs. This may explain why the Met4 distribution becomes more puncta-like when switched from +met to -met condition, when Met32 becomes available inside the nuclei. However, we cannot exclude the possibility that the absence of Met4 LLPS is due to our *in vitro* condition (tag, impurity, lack of post-translational modification, etc.). Met4 is reported to recruit its co-factors including the Mediator and SAGA complex (Leroy et al. 2006), and these factors, together with Pol II and RNA, may affect Met4 condensate formation *in vivo* (Henninger et al. 2021).

TF condensates and the 3D genome topology. TF condensation *in vivo* occurs in a chromatin context, but the relationship between TF condensates and 3D genome topology has not been extensively studied. By recruiting multiple TFs, mediator, and transcription machineries into proximity, TF binding loci can potentially serve as nucleation sites for transcription condensates. Looped enhancers and promoters, as well as clustered genes, may also function as scaffold and stabilize these condensates. This is best illustrated at super-enhancers (SEs), where clustered enhancer sites tend to associate with transcriptional condensates and lead to very high activities of their target genes (Hnisz et al. 2013; Sabari et al. 2018). Synthetic LacO array and endogenous microsatellite repeats were also shown to promote local condensation of associated TFs (Chong et al. 2018). Reversely, TF condensates can mediate long-distance chromosomal interactions by contacting multiple genomic sites and therefore inducing their 3D proximity. This idea is supported by the findings here: 1) multiple Met4-targeted genes are co-localized with Met4 condensates, 2) at least a subset of Met4-targeted genes form clusters with long-distance intra- and inter-chromosomal interactions, and 3) such clustering only occurs in -met activating condition in the presence of Met4. Similar observations were made during yeast heat shock response, where the activator Hsf1 coalesces and mediates transient clustering and activation of heat shock genes (Chowdhary et al. 2019; Chowdhary et al. 2022). A few other mammalian TFs were also shown to contribute to 3D genome conformation. For example,

YAP/TAZ organizes their target sites into clusters that co-localize with the YAP/TAZ/TEAD1 condensates (Lu et al. 2020). NUP98-HOXA9, a chimeric TF related to the pathogenesis of AML, was also shown to mediate long-distance chromosomal loops between NUP98-HOXA9 bound enhancers and oncogenes into SE-like clusters (Ahn et al. 2021).

Interestingly, a *MET3pr* reporter that is associated and activated by Met4 only co-localizes with Met4 puncta when inserted near native Met4 binding sites. Also, adding *MET3pr* reporter gene into these sites does not further increase the local Met4 concentration (**Fig. 6B & C**). These observations indicate that Met4 binding is not *sufficient* for a gene to nucleate or be recruited into a Met4 condensate. The underlying mechanism of this observation is unclear, but we speculate that some properties of the endogenous *MET* genes may facilitate their clustering with Met4 puncta. For example, some *MET* genes, like *MET13* and *MET6*, are associated with nuclear pore complex (NPC) even in the presence of met (Forey et al. 2021). The tethering by NPCs may increase the chance for these genes to come into proximity, enhancing the local density of Met4 target sites to nucleate the Met4 condensates. In contrast, a reporter gene inserted into random genomic locations may not be optimally positioned to contact NPC and/or other Met4 target genes. Further experiments are required to test these ideas. Notably, interaction with NPC was found to be necessary and sufficient to promote clustering of the *GAL1-10* alleles (Brickner et al. 2016).

TF condensates and gene expression. The Met4 condensates represent a local environment with elevated Met4 concentrations, which can promote Met4 binding and lead to enhanced gene expression. Consistent with this idea, *MET3pr* reporter inserted near these Met4 targets, which also co-localizes with the Met4 puncta, shows increased transcriptional activity. Near *MET6*, such hyperactivity of the reporter occurs over a 40kb range. According to previous measurement (Bystricky et al. 2004), 40kb linear chromatin explores a 3D space with ~200 nm diameter, which may reflect the size of the Met4 condensates. The elevation of transcription level is pathway-specific, as *GAL1Spr*-GFP inserted into the same loci does not show the same effect. This finding agrees with the “specialized transcription factory” previously proposed (Bartlett et al. 2006) and argues against a model where the transcription elevation solely relies on general transcription factors like mediator or transcription machinery.

The relation between Met4 condensation and transcriptional activity is further supported by Met4 ΔIDR2.3. This Met4 mutant, in comparison to full length Met4, reduces the Met4 puncta formation and the activities of most of its target genes in the genome. Importantly, ΔIDR2.3 does not have strong effect on the transcriptional activity of *MET3pr* reporter inserted into basal loci, suggesting that this truncation does not directly impact Met4 integrity and its activation function. Instead, it selectively reduces reporter activity at transcriptional hotspots, consistent with the idea that such reduction is due to the disruption of Met4 condensates.

In terms of mechanism, we speculate that 1) high Met4 local concentration inside the condensates may increase the binding rate of Met4, and/or 2) multivalent interactions among Met4, Met32, and possibly other co-activators may slow down the dissociation of Met4 from its target genes. Both ideas are consistent with our observation that Met4 ΔIDR2.3 shows less binding than the full length Met4. The same mechanism has been proposed for other TF condensates, and in some cases, it is supported by direct kinetic evidence (Trojanowski et al. 2022). It should be noted that more TF binding does not necessarily lead to an increase in gene expression level, for example, transcription may be limited by a step downstream of TF binding. Consistent with this idea, a recent study reports that Gal4 condensation facilitates its recruitment to target genes but does not contribute to gene activation (Meeussen et al. 2023). In human cells, artificially enhanced condensation of a TF Ews::Fli1 causes sequestering of this TF into the nucleolus, resulting in decreased expression of their target genes (Chong et al. 2022). This indicates that the exact relation between TF condensates and gene expression relies on the nature of the multivalent interaction, location of condensate formation, transcription kinetics, etc., and it needs to be analyzed on a case-by-case basis.

TF condensates and stress response. The sulfur-containing amino acid methionine is a key metabolite for cell survival, and its depletion represents a major stress for budding yeast. Interestingly, the TFs that were found to form condensates in yeast, include Met4, Gal4, and Hsf1, all respond to certain types of environmental stress. Similar observations are made in higher eukaryotes. For example, YAP forms condensates in response to osmotic stress (Cai et al. 2019; Lu et al. 2020), and phyB in plants uses altered LLPS properties to sense light and temperature cues (Chen et al. 2022). In contrast, constitutive TFs in yeast, like Reb1, Cbf1, and Sth1, are more evenly distributed in the nuclei (**Fig. 1**). The condensation of stress-responding TFs may reflect a functional need to rapidly concentrate related resources into a subset of the

nuclear space for more efficient usage. In the case of Met4, its condensates indeed allow yeast cells to mount a stronger response to met depletion. In addition, TF condensates may accelerate TF target search and response rate, facilitate synchronized expression of target genes, and/or enhance the activation specificity. These potential condensate functions need to be further explored.

Materials and Methods

Plasmid and strain construction. Standard molecular methods were used to construct budding yeast strains and plasmids (**Table S1**). The haploid strain was derived from w303a background, and most genetic modifications here involve homologous recombination. More specifically, to create strains with GFP-tagged endogenous Met4, the *GFP-HIS3* fragment was PCR amplified from a plasmid (pJL1) with primers containing upstream and downstream homologous sequences of the endogenous *MET4* gene. The amplified PCR product was transformed into haploid yeast to insert into the *MET4* locus. A similar strategy was used to create strains with mCherry-tagged endogenous Met32, Met4-TAP, Met32-TAP, Met28-TAP and Cbf1-TAP strains. For strains with tetO-tetR-mCherry labeled loci, variations of plasmid pSR11 were created from containing 196X tetO repeats with flanking homologous sequences to targeted sites were linearized and transformed into Met4-GFP expressing haploid strains. For expression of tetR-mCherry, a plasmid (pMY39) containing the tetR-mCherry insert was linearized and transformed into the *ADE2* genomic locus. To create Met4 truncated strains, individual plasmids containing truncated versions of Met4 (pJL1) were created and were linearized with restriction digestion. The linearized plasmid was then integrated into haploid yeast directly upstream of the *MET4* locus. For endogenous replacement of *MET4* with *MET4* (ΔIDR2.3), a plasmid variant of pJL1 with *MET4* (ΔIDR2.3) was linearized and transformed to replace the endogenous *MET4* gene.

Microscopy and image analysis. For imaging of Met4-GFP and Met32-mCherry, yeast cells were grown in SCD + 10X Met liquid media at 30˚C to OD660 ~ 0.2, washed, and then transferred onto 5 ml of SCD - Met media for 2 hrs for induction. Afterwards the cells were put on a SCD-Met agarose pad and put under the confocal microscope for imaging. Confocal microscopy was performed with Zeiss LSM880 scanning laser confocal (Penn State University Huck Life Sciences Institute) with 488 nm Argon laser (541 nm detection) and 594 nm HeNe laser (648 nm detection) using 63x/1.4 plan apochromat objective. For single cell fluorescent

images, the images were taken with Airyscan detector and deconvoluted with Zen Black software.

The individual nuclei from single cells were segmented to extract the nuclear boundaries and pixel fluorescent information of single nuclei with NucleiSplicer (Matlab) and subsequent nuclei information was analyzed with NucleiAnalyzer (Matlab). Variance and standard deviation were calculated from the nuclear pixels and plotted with OriginPro (**Table S2**). The mean GFP intensities were calculated by subtracting the measure GFP intensities by the mean background intensities of unlabeled cells. Coefficient of Variation (CV) values were calculated by dividing the Std. Dev by the mean GFP values for individual cells. The Fano number was calculated by dividing the Variance by the mean GFP. To normalize the Fano number, the mean Fano number of Free GFP was set to a value of 1 and the rest of the conditions were divided by the mean GFP Fano number (**Table S2**).

Single cell images of yeast cells expressing tetR-mCherry and Met4-GFP were imaged with 10 z-stacks (0.4 µm). The z-stack images of mCherry and GFP channels were analyzed by DotTracker (MATLAB). For individual cells, the program detects the z-stack with the highest mCherry dot intensity. We then either used the GFP image from the same z position (same z) or projected the highest GFP intensity at each pixel for all z positions onto a 2D plane (MIP). The MIP images were aligned with the mCherry dot at the center and averaged among all cells. To calculate the GFP intensities like in Figure 3G and 6C, a single line was drawn across the center and the GFP profile was analyzed by ImageJ.

To measure *S.kud* Met3pr-GFP expression, yeast cells were grown in SCD+10X Met liquid media at 30˚C to OD660 ~ 0.2, washed, and then transferred onto a SCD-Met agarose pad for induction. After 6 hrs, the agarose pad was put under a Leica DMI6000 B fluorescent microscope for imaging. The GFP fluorescent intensity within each cell boundary was quantified using Celltracker4 (MATLAB) (Zou and Bai 2019).

Met4 and Met32 purification. Constructs of Met32-mCherry, and Met4-MBP were inserted into pET28b(+) backbones with an N-terminus 6x-His tag. Met4 and Met32 genes were cloned from budding yeast genomic DNA. MBP-tag was cloned from Addgene CAT#98651 and fusion constructs were assembled using 2xHiFi mastermix (NEB #E2621L) and transformed into DH5a cells (NEB C2987I). A single cysteine sequence was added to the linker between Met4 and

MBP to facilitate maleimide conjugation of fluorophores for imaging. For protein expression, all plasmids were transformed into BL21(DE3)-Sigma32 cells (courtesy of Xin Zhang) and induced according to reported protocol for the Sigma32 cell line (Zhang et al. 2014). Bacterial protein expression was carried out with cells grown in LB supplemented with 50 mg/L kanamycin and 100 mg/L ampicillin at 37ºC to OD_{600}=0.3, induced with 2 g/L arabinose (TCI A0515). Cells were then grown at 30ºC until OD_{600}=0.6, induced with 1% isopropyl b-D-1-thiogalactopyranoside (IPTG, Research Products International I56000) and grown overnight at 20ºC. Cells were resuspended in wash buffer supplemented with 1 mM phenylmethylsulfonyl fluoride (PMSF), and frozen before lysis.

For protein purification, bacterial cells were lysed with sonication and treated with DNaseI and RNaseA according to published protocols for 15 mins (Carrillo et al. 2012). Met32-mCherry was purified using Ni-NTA chromatography (Thermo Scientific HisPur resin #88222) with proteins buffers A (20 mM Tris pH 8.0, 400 mM NaCl, 5 mM imidazole) and B (20 mM Tris pH 8.0, 400 mM NaCl, 250 mM imidazole) with a stepwise gradient of buffer B. Protein was buffer exchanged into buffer C (20 mM HEPES pH 7.5, 400 mM NaCl, 10% glycerol, 1 mM DTT) and concentrated to at least 80 mM using Amicon Pro centrifugal filters 10,000 NMWL (Milipore #ACS501024). The Met4 construct was purified using Ni-NTA chromatography with proteins buffers A and B with a stepwise gradient of buffer B. Ni-NTA elution was immediately loaded onto an amylose column (NEB E8021S) and purified using a stepwise gradient of buffers A and D (20 mM Tris pH 8.0, 400 mM NaCl, 10 mM maltose). Protein was labeled by incubating with 0.8 molar equivalents of Alexa Flour 488 maleimide (Invitrogen A10254). Proteins were buffer exchanged into buffer C and concentrated to less than 50 mM (to avoid aggregation).

Western blot analysis. Met4-MBP samples were run on a 4-20% SDS-PAGE gel (BioRad #4561094). Gels were wet transferred to a PVDF membrane (BioRad #1620177) at 80V for 3 hrs in Tris-Glycine buffer. Transfer was confirmed by Ponceau staining (Sigma P7170-1L). Membrane was blocked with 5% non-fat milk, washed with TBS with 1% Tween 20 (VWR 0777). Membrane was probed with anti-MBP antibody (Thermo Fisher MA527544). Membrane was stripped using PVDF stripping solution (DOT Scientific 65000-500) according to manufacturer instructions and reprobed with anti-6x-His primary antibody (Thermo Fisher MA1-21315) and conducted identically to the first probing. All incubation steps proceeded overnight. Blots were developed using Pierce ECL substrate (Thermo Scientific 32209) with a 2 mins exposure time.

Droplet formation. Proteins were diluted from 400 mM NaCl storage buffer so that the final concentration of the buffer was 150 mM NaCl, 20 mM HEPES pH 7.4, 2% glycerol. Samples were plated on a microscope slide with a hydrophobic spacer (Invitrogen #S24735) between the slide and untreated coverslip. Droplets were allowed to settle for 5 mins prior to imaging. All droplet formation and imaging was conducted at room temperature.

Fluorescent Recovery after Photobleaching (FRAP). Bleaching was conducted after three frames using the 594 nm laser at full power for 45 iterations. Fluorescence intensity was monitored every 3 seconds for a total of 270 seconds per experiment. Fluorescence intensity levels were extracted using Zeiss Zen Black software. Fluorescence intensity was normalized to percent of pre-bleach intensity then averaged. Error bars show +/- SD of the normalized fluorescence intensity. FRAP experiments were conducted at 20 µM Met32-mCherry. Experiments were replicated with at least three preparations of each protein. Snapshots of the bleaching process were processed using FIJI.

Chromatin Immunoprecipitation (ChIP). Yeast strains were grown to OD_{660} of 0.4 in 50 mL of SCD-met medium and crosslinked with 1.39 mL of 37% formaldehyde for 20 mins at room temperature. Crosslinking was quenched by adding 2.7 mL of 2.5 M glycine and incubation for 5 mins. Crosslinked cells were centrifuged at 1882 × *g* for 3 mins at 4°C, and then washed twice with cold 1x Tris-buffer saline (TBS). Cell pellet was then resuspended in 250 µL of fresh FSPP buffer (50 mM HEPES-KOH, pH 7.5, 140 mM NaCl, 1 mM EDTA, 1% Triton X-100, 0.1% sodium deoxycholate, 1% protease inhibitor cocktail, and 1 mM phenylmethylsulfonyl fluoride (PMSF) and vortexed with ~300 µL glass beads for 2 cycles of 20 mins with an intervening 10 mins in a 4°C cold room. Another 250 µL of fresh FSPP was added to each sample, and the cap and bottom of tubes were punched with a hot needle so that cell lysate could be collected by centrifuging at 836 × *g* for 5 mins at 4°C. FSPP (0.5 mL) was added to the cell lysate to resuspend the pellet. The cell lysate was then sonicated using a 30 s on 30 s off cycle at 4°C for 7 cycles. Sonicated cell lysate was transferred to 1.5 mL tube and centrifuged at 17,136 × *g* for 20 mins at 4°C. Two hundred microliters of supernatant was saved as input. Another 400 µL of supernatant was mixed with 600 µL of FSPP buffer and 20 µL of pre-blocked Magnetic IgG beads and TAP antibody (Thermo CAB1001) or Rpb3 antibody (Biolegend 920204) for 10–12 hrs at 4ºC. Chromatin was incubated with the beads overnight at 4°C, and then washed

sequentially at 4°C with 1xFA-lysis buffer (50 mM HEPES-KOH, pH 7.5, 140 mM NaCl, 1 mM EDTA, 1% Triton X-100, 0.1% sodium deoxycholate), 1xFA-lysis buffer containing 150 mM NaCl, 1xFA-lysis buffer containing 500 mM NaCl, LiCl buffer (0.25 M LiCl, 1% NP-40, 1% sodium deoxycholate, 1 mM EDTA, and 10 mM Tris-HCl pH 8.0), and lastly TE buffer, pH 8.0. Chromatin was then eluted with 400 µL ChIP elution buffer (50 mM NaCl, 50 mM Tris-HCl, pH 8.0, 10 mM EDTA, 1% SDS). Samples were mixed by rotation at 30°C for 30 mins. Beads were pelleted by centrifugation at 17,136 × *g* and discarded. Five microliters of 20 mg/mL Proteinase K was added to supernatant; 180 µL of 1xFA-lysis buffer, 20 µL of 10% SDS and 5 µL of 20 mg/mL Proteinase K were added into the input samples. ChIP and input samples were then incubated overnight at 65°C to reverse crosslinking. DNA was extracted by phenol:chloroform:isoamyl alcohol (25:24:1) followed by ethanol precipitation. Input samples were then treated with 200 µg RNase A and precipitated with ethanol after adding 20 µg glycogen. Enrichments of target TFs were quantified by quantitative PCR (qPCR). All ChIP experiments were done in biological duplicates.

RNA-seq. Cells were grown in 5 ml of SCD +10x met overnight. 5 ml of fresh SCD +10x was innoculated with 5 µl of saturated culture until OD_{660} ~0.2. The culture is collected by centrifugation and washed 3x with sterile H2O. The collected culture is then grown in SCD -met media for 2 hrs to reach OD_{660} ~0.4 and centrifuged at 300g for 4 mins at RT. The pellet was washed twice with sterile H2O and resuspended in 250 µl of RNA lysis buffer (10mM Tris-HCl pH8.5, 5mM EDTA, 2% SDS, 2% stock 2-mercaptoethanol) and placed on a heat block at 85ºC for 20 mins mixing every 2 mins. The mixture was centrifuged at 12,000g for 5 mins and the supernatant was transferred to a new tube. The supernatant was then mixed with 1 ml of trizol and heated at 65ºC for 20 mins with mixing in between. Standard trizol/chloroform RNA extraction protocol was followed. The extracted RNA was analyzed with Tapestation to check their integrity. RNA with RIN (>7.5) was used for downstream analysis. Messenger RNA was captured using RNA purification beads (NEB). The eluted mRNA was fragmented and denatured for first and second strand synthesis for conversion into cDNA. The sequencing libraries were constructed using conventional protocols (NEB).

Methyltransferase Targeting-based chromosome Architecture Capture (MTAC). Yeast cells were grown in 50 ml SCD +10x Met media at OD_{660} 0.3. The cells were centrifuged and washed 3 times with autoclaved H_2O before transfer to 50 ml of SCD-Met and induced with 2

nM β-eastradiol for 2 hrs. After induction the cells were centrifuged at 4000g for 5 mins and collected in 800 µl of TE and 200 µl lysis buffer (0.5 M EDTA pH 8.0, 1 M Tris pH 8.0, 10% SDS) and incubated at 65 ºC for 30 mins. The cell lysate (1ml) was then sonicated using a 30 s on 30 s off cycle at 4°C for 11 cycles. The sonicated lysate was centrifuged at 12,000g at 4 ºC for 20 mins and the supernatant was transferred to a new tube. The supernatant was mixed with 500 µl for Phenol:Chloroform:Isoamyl Alcohol (25:24:1) nucleic acid extraction. The methylated genomic DNA (5 µg) was incubated with 2 µg of anti-methylcytosine antibody in 1X IP buffer on a rotating platform 4°C for 8-12 hrs. Input DNA (1%, 50 ng) was set aside for normalization. The lysate/antibody complex was incubated with protein A/G agarose beads for 2 hrs and washed 3x with 1x IP buffer. The beads were resuspended with 210 µl digestion buffer and incubated on a rotating platform at 55 ºC for 2 hrs. The eluted DNA was precipitated in 1 ml of ethanol and 3 µl glycogen (20mg/ml) and eluted in 60 µl of TE.

For strains with Met4 Auxin-induced degradation, we tagged the endogenous Met4 protein with V5-AID (Met4-V5-AID) and introduced OsTIR1 to the cells. Depletion of the Met4 was achieved by adding auxin (Sigma, I2886) to a final concentration of 500 µM. Strains were incubated with auxin for 30 mins prior to MTAC experiment. Depletion was confirmed by western blot.

Data availability

All sequencing data in this study can be accessed on GEO series GSE252386, which include 1) GSE252384: ChIP-seq raw data (fastq), bed files, and bigWig files, 2) GSE252385: RNA-seq raw data (fastq), counts data (featureCounts), and DESeq2 tables, and 3) GSE252985: MTAC raw data (fastq), bigWig files, counts data (featureCounts) and DESeq2 tables.

Acknowledgements

We thank Dr. Joseph Reese for providing auxin-inducible degron plasmids and yeast strains. We acknowledge all members in the Bai lab for insightful comments on the manuscript. We thank the Microscopy Facility and the CSL Behring Fermentation Facility at Penn State for their help with imaging and protein purification. We are grateful to Dr. Cheryl Keller at the Genomics Research Incubator at the Huck Institutes of the Life Sciences for helping with the genomic

assays. We also want to thank the members of the Center of Eukaryotic Gene Regulation at PSU for discussions and technical support. This work is supported by the National Institutes of Health (R35 GM139654 to L.B.) and National Science Foundation (MCB- 2016266 to L.B.).

Author Contributions

L.B., J.L., L.S. and Y.L. designed the experiments; J.L. performed most of the experiments and data analysis with help from S.B.; L.S. and Y.L. carried out most of the experiments in Fig. 2 and Fig. 4, respectively; F.Z. contributed to the image data analysis; X.Z. helped with protein purification; J.L. and L.B. wrote the manuscript.

Conflict of Interest Statement

The authors declare no conflict of interest.

Figure Legends

Figure 1. The trans-activator Met4 and its co-factor Met32 form puncta in the nucleus. A) Representative images of Met4-GFP in ± methionine (met) conditions. Control cells expressing free GFP (driven by the *HOpr*), Cbf1-GFP, Reb1-GFP, and Sth1-GFP cells are shown with similar contrasts. Scale bars represent 4μm (same as in D & G). **B & C)** The mean coefficient of variance (CV) and Fano numbers of nuclear pixel intensities for different versions of GFPs in panel A. The Fano numbers are normalized so that the free GFP has a Fano number 1. Significance was calculated in comparison with free GFP values using two-tailed Student's t-test (***: $p<0.001$). Number of cell analyzed: Met4-GFP +/-met (65/147), free GFP (67), Cbf1 (48), Reb1 (50), Sth1 (59). **D)** Representative images of strains expressing Met32-mCherry in +/- met conditions. Control strain expressing free mCherry (driven by the *HOpr*) is shown with similar contrasts. **E & F)** The mean CV and normalized Fano number of pixel intensities of Met32-mCherry vs free mCherry. **G)** Representative images of strains co-expressing Met4-GFP and Met32-mCherry (top row), or Sth1-GFP and Met32-mCherry (bottom row). **H)** A histogram of

Pearson correlation coefficient between co-expressed Met4-GFP and Met32-mCherry signals (red bars *N*=93) or Sth1-GFP and Met32-mCherry signals (black bars *N*=149) in each cell.

Figure 2. Met32 forms condensates with LLPS properties *in vitro*. A) Probabilities of individual Met TFs (Met4, Met32, Met31, Met28), GFP, and mCherry to undergo liquid-liquid phase separation from a published prediction program (Fuzdrop). **B)** Coomassie staining and western blots of purified Met4 and Met32 proteins. **C)** Protein aggregate and droplet formation observed for Met4-MBP and Met32-mCherry fusion proteins. Met4 and GFP are 5 µM, Met32-mCherry and mCherry are 10 µM in 20 mM HEPES pH 7.5, 150 mM NaCl buffer. Met4 and GFP are in 20 mM HEPES pH 7.5, 150 mM NaCl or 50 mM NaCl. Met4 is labeled with Alexa 488 (AF488). Scale bar represent 10 µm (same as in D-F). **D)** Merging of Met32-mCherry droplets. Met32-mCherry is at 30 µM in 20 mM HEPES pH 7.5, 150 mM NaCl. **E)** Fluorescence recovery after photobleaching (FRAP) data for 20 µM Met32 droplets. The intensity data was collected every 3 seconds for 270 seconds and normalized to percent bleaching. Inset: Representative images of Met32 FRAP. **F)** Colocalization of Met32-mCherry droplets (10 µM) with Met4-MBP (5 µM) in 150 mM NaCl.

Figure 3. Met4-activated genes co-localize with Met4 puncta. A) Model of Met4 condensate in the chromatin context. Upon met depletion, Met TFs may form condensates that interact with multiple target genes, leading to the 3D clustering of these co-regulated genes. **B)** Examples of ChIP-seq signals of Met TFs (Met4, Met32, Met28 and Cbf1) in ±met conditions. The Met TF co-binding peak shown here is near the *MET13* gene. **C)** Heatmaps of Met4, Met32, Met28, and Cbf1 ChIP-seq peaks in ± met conditions. The peaks were clustered into ones enriched with all four Met TFs (*N* = 34), enriched with Met4 and Cbf1 (*N* = 11), and enriched with Cbf1 only (*N* = 107). **D)** Volcano plot of RNA-seq data comparing mRNA levels in ± met conditions. Most genes near Met TFs co-binding peaks are strongly induced by met depletion (red dots). **E)** Single nuclei images of yeast cells expressing Met4-GFP and TetR-mCherry with a TetO array integrated near *MET13 / MET6* (Met4 targets), or *MAT / PUT1 (*non-targeted *c*ontrol). Images were taken with 14 z-stacks with step size 0.4 µm. Max intensity projection ("MIP") and "same Z" show Met4-GFP images with either maximum intensity projection among all z stacks, or with a single stack at the same z plane as "mCherry", where the mCherry labeled TetO array shows the highest intensity. "merged" is the merged image of the "same Z" and the "mCherry". Scale bars represent 1µm (same as in F). **F)** MIP of mCherry and GFP intensities. Images of each cell are aligned and centered with the mCherry dot, which represents the TetO array, and the

corresponding GFP MIPs for all cells are averaged. Number of cell analyzed: *MET13* +/-met (447/413), *MET6* (381), *MAT* +met/-met (290/424), *PUT1* (524). **G)** The GFP intensity profiles of the averaged MIP images shown in F. A line was drawn across the dot center and the GFP intensity was calculated along the line. The GFP intensity near the dot center is significantly higher for *MET13 / MET6* loci in -met condition than *PUT1* and *MAT*. Significance was calculated using two-tailed Student's t-test (***: $p<0.001$).

Figure 4. Met4-dependent clustering of *MET* genes upon induction. A) MTAC workflow. In a "targeted" MTAC strain, a LacO array is integrated into a genomic locus (viewpoint, VP) and recruits LacI-M.CviPI, an ectopic DNA methyltransferase that methylates the cytosine in a "GC" dinucleotide in proximal DNA. LacI-M.CviPI is also expressed in a control strain with no LacO array insertion (background methylation). Methylation in these two strains is detected by ChIP, and methylation level in nucleosome-depleted regions (NDRs) are compared in targeted vs control strains. Significantly higher methylation in the targeted strain indicates proximity to the VP. **B)** VP design of the *MET13* locus. **C)** Volcano plot of MTAC signals with *MET13* as VP in ±met conditions. Each dot represents an individual NDR, and colored dots are the NDRs that show proximity to the VP (significantly higher methylation in the targeted vs control strains). Local (intra-chromosomal interactions within 30kb), far-cis (intra-chromosomal interactions over 30kb), and trans (inter-chromosomal interactions) are shown in blue, green, and orange. Same as below. **D)** Design of Met4 depletion assay. Met4 is depleted by auxin-degron system in ±met conditions, resulting in four conditions: (1) +met, -IAA, (2) -met, -IAA, (3) +met, +IAA, (4) -met, +IAA. β-estradiol is added in all conditions to induce the expression of LacI-M.CviPI. **E)** Volcano plot of MTAC signals with *MET6* as VP for the four conditions in panel D. Note that long-distance interactions are detected in condition (2) but are largely absent in other three conditions. **F)** MTAC and Met4 ChIP-seq data at the *MET6* locus (VP) and *MUP1, STR3* and *YKG9* as interacting regions of the VP. MTAC signal is shown in the four conditions in panel D. The ChIP enrichment of Met4 is shown in ±met conditions. *P,* FDR-adjusted *P* value, Wald test by DESeq2. ns, non-significant.

Figure 5. Characterization of a *MET* "transcriptional hotspot" in haploid yeast. A) Schematic of strains constructed with *S.kud MET3pr*-GFP reporter inserted near the *MET13* transcriptional hotspot (*CWC23, RSM23*) and "basal" loci (*ATG36, LDS2*). **B & C)** Mean cellular GFP fluorescent intensities and GFP mRNA measured by qRT-PCR in the four strains above in ±met conditions. **D)** ChIP-qPCR of Rpb1 over the GFP ORF in the four strains above in -met. **E**

& F) ChIP-qPCR of Met32 and Met4 over the *S.kud MET3pr* in the four strains above in -met. The asterisks represent *: <0.05, **: <0.01, ***: <0.001. Same as below.

Figure 6. Reporter activities near Met4 binding sites are enhanced over a ~40kb range. A) Schematics of measuring the co-localization of the GFP reporter with Met4 puncta. *S.kud MET3pr*-fsGFP (frameshifted GFP) reporter gene and a tetO array (196x) are inserted side by side into the genome, in this case near the *MET6* gene. **B)** Averaged MIPs of mCherry and GFP intensities near *MET6* (Met4 target) and *PUT1* / *ATG36* (not Met4 targets) in the presence of nearby reporter. These images are generated using the same method as in Figure 3F. Scale bars represent 1µm. **C)** The GFP intensity profile across the dot center in panel B. For *MET6* and *PUT1,* the same type of data without the GFP reporter (-rep) are also included. Number of cells analyzed (for panel B & C): *PUT1* +/-rep (318/524), *ATG36* +rep (386), *MET6* +/-rep (330/381). **D)** Schematic of GFP reporter insertion near three additional Met4-bound loci, *MET17, RMD6, and MET6*. The distance and orientation of the insertion are labeled in the diagram. **E)** Mean GFP fluorescent intensities when *S.kud MET3pr*-GFP are inserted near indicated genes. The genes labeled in red have adjacent Met4-bound sites, while the ones labeled in grey do not. **F)** Same as in panel E except with *MET17pr*-GFP and *GAL1Spr*-GFP reporter. Strains with *MET17pr*-GFP were grown in -met, and the ones with *GAL1Spr*-GFP were pre-grown in raffinose and induced by galactose for 6 hours. **G)** Schematic of the *MET3pr*-GFP reporter inserted at various distances from the Met4 binding site near the *MET6* gene. The same orientation was used for all the loci as indicated. **H)** Mean GFP fluorescent intensities with *MET3pr*-GFP and *GAL1Spr*-GFP reporters inserted into locations indicated in panel G, in comparison to the same reporter inserted into two control loci far from Met4 binding sites.

Figure 7. The deletion of a disordered region in Met4 reduces puncta formation and reporter expression at transcriptional hotspots. A) PONDR disorder plot of Met4 with previously annotated functional domains, including activation domain (aa95-144) that interacts with mediator, inhibitory domain (aa188-235), auxiliary domain (aa312-375) that interacts with Met31/32, and bZIP domain (aa595-660) that interacts with Cbf1. **B)** Single nuclei images of cells expressing full length Met4 (±met) or Met4 with various truncations (-met) fused with GFP. **C)** The Fano numbers of nuclear pixel intensities for different versions of GFPs in panel B. Number of cell analyzed: Met4GFP +/-met (65/147), Free GFP (67), ΔIDR1/2/3 (172/95/172), ΔIDR2.1/2.2/2.3 (134/177/161). **D)** Heatmaps of full length Met4 and Met4 ΔIDR2.3 ChIP-seq in –met over previously identified Met TF binding sites. **E)** Alignment counts underneath the Met

TF ChIP-seq peaks over the same sites for TAP tagged full length Met4 and Met4 ΔIDR2.3 (sorted from high to low). **F)** Volcano plot from RNA-seq data from cells containing full length Met4 or Met4 Δ IDR2.3 in -met. Genes associated with Met TFs (Fig. 3C) are indicated in red. **G)** Mean GFP intensities from cells expressing full length Met4 and Met4 ΔIDR2.3 with *MET3pr*-GFP reporter inserted into loci near (red) or far away from (black) Met4-target genes. The dashed lines represent basal reporter expression.

References

Ahn JH, Davis ES, Daugird TA, Zhao S, Quiroga IY, Uryu H, Li J, Storey AJ, Tsai YH, Keeley DP et al. 2021. Phase separation drives aberrant chromatin looping and cancer development. *Nature* **595**: 591-595.

Apostolou E, Thanos D. 2008. Virus Infection Induces NF-kappaB-dependent interchromosomal associations mediating monoallelic IFN-beta gene expression. *Cell* **134**: 85-96.

Banani SF, Lee HO, Hyman AA, Rosen MK. 2017. Biomolecular condensates: organizers of cellular biochemistry. *Nat Rev Mol Cell Biol* **18**: 285-298.

Bartlett J, Blagojevic J, Carter D, Eskiw C, Fromaget M, Job C, Shamsher M, Trindade IF, Xu M, Cook PR. 2006. Specialized transcription factories. *Biochem Soc Symp* doi:10.1042/bss0730067: 67-75.

Blaiseau PL, Thomas D. 1998. Multiple transcriptional activation complexes tether the yeast activator Met4 to DNA. *EMBO J* **17**: 6327-6336.

Boeynaems S, Alberti S, Fawzi NL, Mittag T, Polymenidou M, Rousseau F, Schymkowitz J, Shorter J, Wolozin B, Van Den Bosch L et al. 2018. Protein Phase Separation: A New Phase in Cell Biology. *Trends Cell Biol* **28**: 420-435.

Boija A, Klein IA, Sabari BR, Dall'Agnese A, Coffey EL, Zamudio AV, Li CH, Shrinivas K, Manteiga JC, Hannett NM et al. 2018. Transcription Factors Activate Genes through the Phase-Separation Capacity of Their Activation Domains. *Cell* **175**: 1842-1855.e1816.

Brickner DG, Sood V, Tutucci E, Coukos R, Viets K, Singer RH, Brickner JH. 2016. Subnuclear positioning and interchromosomal clustering of the GAL1-10 locus are controlled by separable, interdependent mechanisms. *Mol Biol Cell* **27**: 2980-2993.

Bystricky K, Heun P, Gehlen L, Langowski J, Gasser SM. 2004. Long-range compaction and flexibility of interphase chromatin in budding yeast analyzed by high-resolution imaging techniques. *Proc Natl Acad Sci U S A* **101**: 16495-16500.

Cai D, Feliciano D, Dong P, Flores E, Gruebele M, Porat-Shliom N, Sukenik S, Liu Z, Lippincott-Schwartz J. 2019. Phase separation of YAP reorganizes genome topology for long-term YAP target gene expression. *Nat Cell Biol* **21**: 1578-1589.

Cai M, Davis RW. 1990. Yeast centromere binding protein CBF1, of the helix-loop-helix protein family, is required for chromosome stability and methionine prototrophy. *Cell* **61**: 437-446.

846 Carrillo E, Ben-Ari G, Wildenhain J, Tyers M, Grammentz D, Lee TA. 2012. Characterizing the roles of
847 Met31 and Met32 in coordinating Met4-activated transcription in the absence of Met30. *Mol*
848 *Biol Cell* **23**: 1928-1942.
849 Carter DR, Eskiw C, Cook PR. 2008. Transcription factories. *Biochem Soc Trans* **36**: 585-589.
850 Chen D, Lyu M, Kou X, Li J, Yang Z, Gao L, Li Y, Fan LM, Shi H, Zhong S. 2022. Integration of light and
851 temperature sensing by liquid-liquid phase separation of phytochrome B. *Mol Cell* **82**: 3015-
852 3029.e3016.
853 Chong S, Dugast-Darzacq C, Liu Z, Dong P, Dailey GM, Cattoglio C, Heckert A, Banala S, Lavis L, Darzacq X
854 et al. 2018. Imaging dynamic and selective low-complexity domain interactions that control gene
855 transcription. *Science* **361**.
856 Chong S, Graham TGW, Dugast-Darzacq C, Dailey GM, Darzacq X, Tjian R. 2022. Tuning levels of low-
857 complexity domain interactions to modulate endogenous oncogenic transcription. *Mol Cell* **82**:
858 2084-2097.e2085.
859 Chowdhary S, Kainth AS, Paracha S, Gross DS, Pincus D. 2022. Inducible transcriptional condensates
860 drive 3D genome reorganization in the heat shock response. *Mol Cell* **82**: 4386-4399.e4387.
861 Chowdhary S, Kainth AS, Pincus D, Gross DS. 2019. Heat Shock Factor 1 Drives Intergenic Association of
862 Its Target Gene Loci upon Heat Shock. *Cell Rep* **26**: 18-28.e15.
863 Dignon GL, Best RB, Mittal J. 2020. Biomolecular Phase Separation: From Molecular Driving Forces to
864 Macroscopic Properties. *Annu Rev Phys Chem* **71**: 53-75.
865 Donovan BT, Chen H, Eek P, Meng Z, Jipa C, Tan S, Bai L, Poirier MG. 2023. Basic helix-loop-helix pioneer
866 factors interact with the histone octamer to invade nucleosomes and generate nucleosome-
867 depleted regions. *Mol Cell* **83**: 1251-1263.e1256.
868 Donovan BT, Chen H, Jipa C, Bai L, Poirier MG. 2019. Dissociation rate compensation mechanism for
869 budding yeast pioneer transcription factors. *Elife* **8**.
870 Du M, Bai L. 2017. 3D clustering of co-regulated genes and its effect on gene expression. *Curr Genet* **63**:
871 1017-1021.
872 Du M, Zhang Q, Bai L. 2017. Three distinct mechanisms of long-distance modulation of gene expression
873 in yeast. *PLoS Genet* **13**: e1006736.
874 Fanucchi S, Shibayama Y, Burd S, Weinberg MS, Mhlanga MM. 2013. Chromosomal contact permits
875 transcription between coregulated genes. *Cell* **155**: 606-620.
876 Forey R, Barthe A, Tittel-Elmer M, Wery M, Barrault MB, Ducrot C, Seeber A, Krietenstein N, Szachnowski
877 U, Skrzypczak M et al. 2021. A Role for the Mre11-Rad50-Xrs2 Complex in Gene Expression and
878 Chromosome Organization. *Mol Cell* **81**: 183-197.e186.
879 Fullwood MJ, Liu MH, Pan YF, Liu J, Xu H, Mohamed YB, Orlov YL, Velkov S, Ho A, Mei PH et al. 2009. An
880 oestrogen-receptor-alpha-bound human chromatin interactome. *Nature* **462**: 58-64.
881 Hatos A, Tosatto SCE, Vendruscolo M, Fuxreiter M. 2022. FuzDrop on AlphaFold: visualizing the
882 sequence-dependent propensity of liquid-liquid phase separation and aggregation of proteins.
883 *Nucleic Acids Res* **50**: W337-W344.
884 Henninger JE, Oksuz O, Shrinivas K, Sagi I, LeRoy G, Zheng MM, Andrews JO, Zamudio AV, Lazaris C,
885 Hannett NM et al. 2021. RNA-Mediated Feedback Control of Transcriptional Condensates. *Cell*
886 **184**: 207-225.e224.
887 Hnisz D, Abraham BJ, Lee TI, Lau A, Saint-André V, Sigova AA, Hoke HA, Young RA. 2013. Super-
888 enhancers in the control of cell identity and disease. *Cell* **155**: 934-947.
889 Ju QD, Morrow BE, Warner JR. 1990. REB1, a yeast DNA-binding protein with many targets, is essential
890 for growth and bears some resemblance to the oncogene myb. *Mol Cell Biol* **10**: 5226-5234.

891 Jumper J, Evans R, Pritzel A, Green T, Figurnov M, Ronneberger O, Tunyasuvunakool K, Bates R, Žídek A,
892 Potapenko A et al. 2021. Highly accurate protein structure prediction with AlphaFold. *Nature*
893 **596**: 583-589.
894 Kuras L, Barbey R, Thomas D. 1997. Assembly of a bZIP-bHLH transcription activation complex:
895 formation of the yeast Cbf1-Met4-Met28 complex is regulated through Met28 stimulation of
896 Cbf1 DNA binding. *EMBO J* **16**: 2441-2451.
897 Kuras L, Cherest H, Surdin-Kerjan Y, Thomas D. 1996. A heteromeric complex containing the centromere
898 binding factor 1 and two basic leucine zipper factors, Met4 and Met28, mediates the
899 transcription activation of yeast sulfur metabolism. *EMBO J* **15**: 2519-2529.
900 Kuras L, Thomas D. 1995. Functional analysis of Met4, a yeast transcriptional activator responsive to S-
901 adenosylmethionine. *Mol Cell Biol* **15**: 208-216.
902 Lee TA, Jorgensen P, Bognar AL, Peyraud C, Thomas D, Tyers M. 2010. Dissection of combinatorial
903 control by the Met4 transcriptional complex. *Mol Biol Cell* **21**: 456-469.
904 Leroy C, Cormier L, Kuras L. 2006. Independent recruitment of mediator and SAGA by the activator Met4.
905 *Mol Cell Biol* **26**: 3149-3163.
906 Li G, Ruan X, Auerbach RK, Sandhu KS, Zheng M, Wang P, Poh HM, Goh Y, Lim J, Zhang J et al. 2012.
907 Extensive promoter-centered chromatin interactions provide a topological basis for
908 transcription regulation. *Cell* **148**: 84-98.
909 Li Y, Lee J, Bai L. 2024. DNA methylation-based high-resolution mapping of long-distance chromosomal
910 interactions in nucleosome-depleted regions. *Nat Commun* **15**: 4358.
911 Lim B, Levine MS. 2021. Enhancer-promoter communication: hubs or loops? *Curr Opin Genet Dev* **67**: 5-9.
912 Lu Y, Wu T, Gutman O, Lu H, Zhou Q, Henis YI, Luo K. 2020. Phase separation of TAZ compartmentalizes
913 the transcription machinery to promote gene expression. *Nat Cell Biol* **22**: 453-464.
914 Lyons H, Veettil RT, Pradhan P, Fornero C, De La Cruz N, Ito K, Eppert M, Roeder RG, Sabari BR. 2023.
915 Functional partitioning of transcriptional regulators by patterned charge blocks. *Cell* **186**: 327-
916 345.e328.
917 McSwiggen DT, Mir M, Darzacq X, Tjian R. 2019. Evaluating phase separation in live cells: diagnosis,
918 caveats, and functional consequences. *Genes Dev* **33**: 1619-1634.
919 Meeussen JVW, Pomp W, Brouwer I, de Jonge WJ, Patel HP, Lenstra TL. 2023. Transcription factor
920 clusters enable target search but do not contribute to target gene activation. *Nucleic Acids Res*
921 **51**: 5449-5468.
922 Menant A, Baudouin-Cornu P, Peyraud C, Tyers M, Thomas D. 2006. Determinants of the ubiquitin-
923 mediated degradation of the Met4 transcription factor. *J Biol Chem* **281**: 11744-11754.
924 Mir M, Stadler MR, Ortiz SA, Hannon CE, Harrison MM, Darzacq X, Eisen MB. 2018. Dynamic multifactor
925 hubs interact transiently with sites of active transcription in. *Elife* **7**.
926 Misteli T. 2020. The Self-Organizing Genome: Principles of Genome Architecture and Function. *Cell* **183**:
927 28-45.
928 Mumberg D, Muller R, Funk M. 1994. Regulatable promoters of Saccharomyces cerevisiae: comparison
929 of transcriptional activity and their use for heterologous expression. *Nucleic Acids Res* **22**: 5767-
930 5768.
931 Nott TJ, Petsalaki E, Farber P, Jervis D, Fussner E, Plochowietz A, Craggs TD, Bazett-Jones DP, Pawson T,
932 Forman-Kay JD et al. 2015. Phase transition of a disordered nuage protein generates
933 environmentally responsive membraneless organelles. *Mol Cell* **57**: 936-947.
934 Okada M, Fujimoto M, Srivastava P, Pandey A, Takii R, Nakai A. 2023. The Mediator subunit MED12
935 promotes formation of HSF1 condensates on heat shock response element arrays in heat-
936 shocked cells. *FEBS Lett* **597**: 1702-1717.

937 Oluwadare O, Highsmith M, Cheng J. 2019. An Overview of Methods for Reconstructing 3-D
938 Chromosome and Genome Structures from Hi-C Data. *Biol Proced Online* **21**: 7.
939 Ouni I, Flick K, Kaiser P. 2010. A transcriptional activator is part of an SCF ubiquitin ligase to control
940 degradation of its cofactors. *Mol Cell* **40**: 954-964.
941 Rieder D, Trajanoski Z, McNally JG. 2012. Transcription factories. *Front Genet* **3**: 221.
942 Sabari BR, Dall'Agnese A, Boija A, Klein IA, Coffey EL, Shrinivas K, Abraham BJ, Hannett NM, Zamudio AV,
943 Manteiga JC et al. 2018. Coactivator condensation at super-enhancers links phase separation
944 and gene control. *Science* **361**.
945 Schoenfelder S, Fraser P. 2019. Long-range enhancer-promoter contacts in gene expression control. *Nat*
946 *Rev Genet* **20**: 437-455.
947 Shin Y, Berry J, Pannucci N, Haataja MP, Toettcher JE, Brangwynne CP. 2017. Spatiotemporal Control of
948 Intracellular Phase Transitions Using Light-Activated optoDroplets. *Cell* **168**: 159-171.e114.
949 Sutherland H, Bickmore WA. 2009. Transcription factories: gene expression in unions? *Nat Rev Genet* **10**:
950 457-466.
951 Thomas D, Jacquemin I, Surdin-Kerjan Y. 1992. MET4, a leucine zipper protein, and centromere-binding
952 factor 1 are both required for transcriptional activation of sulfur metabolism in Saccharomyces
953 cerevisiae. *Mol Cell Biol* **12**: 1719-1727.
954 Thomas D, Surdin-Kerjan Y. 1997. Metabolism of sulfur amino acids in Saccharomyces cerevisiae.
955 *Microbiol Mol Biol Rev* **61**: 503-532.
956 Trojanowski J, Frank L, Rademacher A, Mücke N, Grigaitis P, Rippe K. 2022. Transcription activation is
957 enhanced by multivalent interactions independent of phase separation. *Mol Cell* **82**: 1878-
958 1893.e1810.
959 Uyehara CM, Apostolou E. 2023. 3D enhancer-promoter interactions and multi-connected hubs:
960 Organizational principles and functional roles. *Cell Rep* **42**: 112068.
961 Vendruscolo M, Fuxreiter M. 2022. Sequence Determinants of the Aggregation of Proteins Within
962 Condensates Generated by Liquid-liquid Phase Separation. *J Mol Biol* **434**: 167201.
963 Whyte WA, Orlando DA, Hnisz D, Abraham BJ, Lin CY, Kagey MH, Rahl PB, Lee TI, Young RA. 2013. Master
964 transcription factors and mediator establish super-enhancers at key cell identity genes. *Cell* **153**:
965 307-319.
966 Xue B, Dunbrack RL, Williams RW, Dunker AK, Uversky VN. 2010. PONDR-FIT: a meta-predictor of
967 intrinsically disordered amino acids. *Biochim Biophys Acta* **1804**: 996-1010.
968 Yan C, Chen H, Bai L. 2018. Systematic Study of Nucleosome-Displacing Factors in Budding Yeast. *Mol*
969 *Cell* **71**: 294-305.e294.
970 Zhang D, Bai L. 2016. Interallelic interaction and gene regulation in budding yeast. *Proc Natl Acad Sci U S*
971 *A* **113**: 4428-4433.
972 Zhang H, Shao S, Zeng Y, Wang X, Qin Y, Ren Q, Xiang S, Wang Y, Xiao J, Sun Y. 2022. Reversible phase
973 separation of HSF1 is required for an acute transcriptional response during heat shock. *Nat Cell*
974 *Biol* **24**: 340-352.
975 Zhang X, Liu Y, Genereux JC, Nolan C, Singh M, Kelly JW. 2014. Heat-shock response transcriptional
976 program enables high-yield and high-quality recombinant protein production in Escherichia coli.
977 *ACS Chem Biol* **9**: 1945-1949.
978 Zhao J, Faryabi RB. 2023. Spatial promoter-enhancer hubs in cancer: organization, regulation, and
979 function. *Trends Cancer* doi:10.1016/j.trecan.2023.07.017.
980 Zhu I, Song W, Ovcharenko I, Landsman D. 2021. A model of active transcription hubs that unifies the
981 roles of active promoters and enhancers. *Nucleic Acids Res* **49**: 4493-4505.
982 Zou F, Bai L. 2019. Using time-lapse fluorescence microscopy to study gene regulation. *Methods* **159-160**:
983 138-145.

984

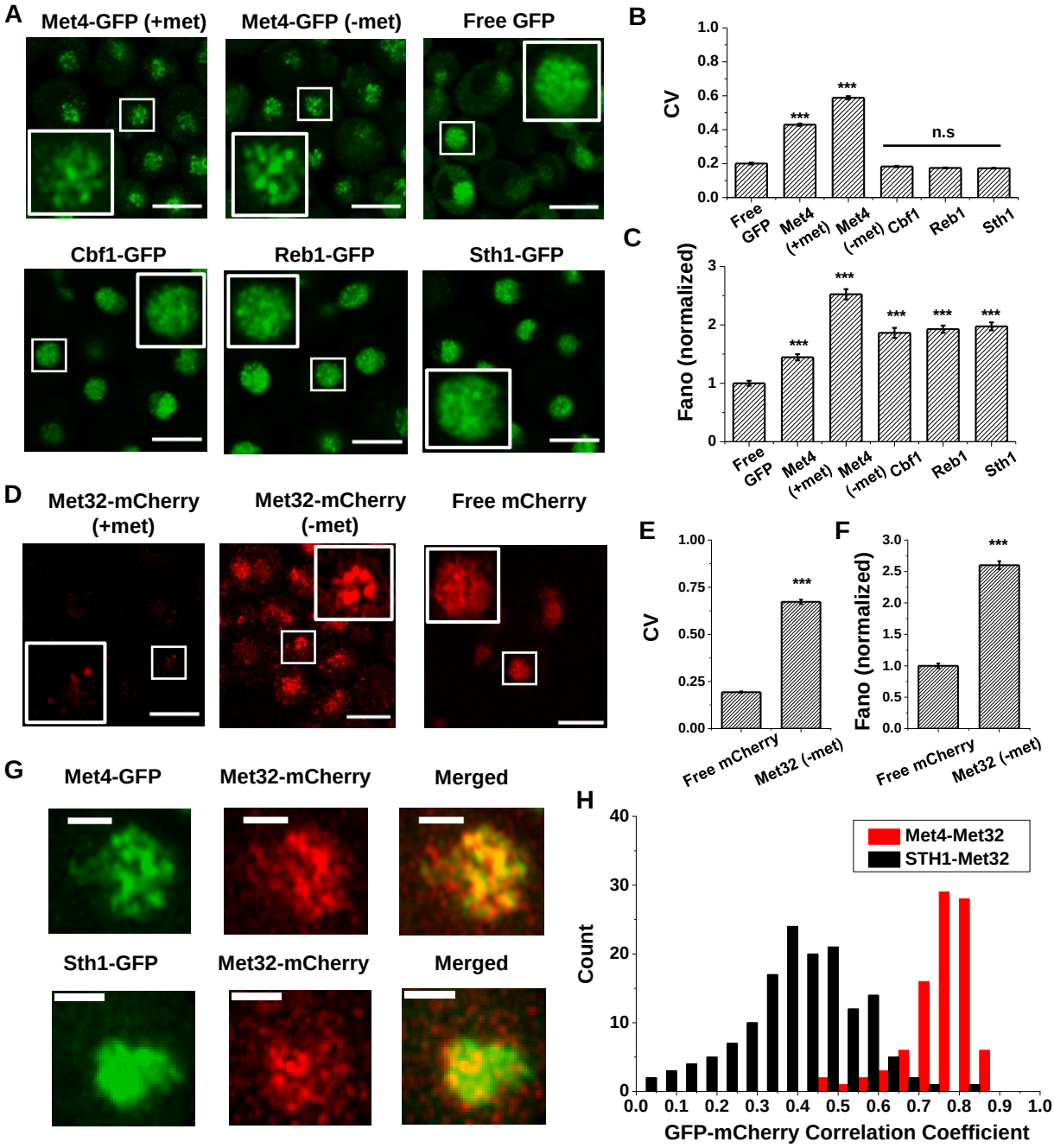
A
Met4-GFP (+met)
Met4-GFP (-met)
Free GFP
Cbf1-GFP
Reb1-GFP
Sth1-GFP
B
CV
1.0
0.8
0.6
0.4
0.2
0.0
***
***
n.s
Free GFP
Met4 (+met)
Met4 (-met)
Cbf1
Reb1
Sth1
C
Fano (normalized)
3
2
1
0
***
***
***
***
***
Free GFP
Met4 (+met)
Met4 (-met)
Cbf1
Reb1
Sth1
D
Met32-mCherry (+met)
Met32-mCherry (-met)
Free mCherry
E
CV
1.00
0.75
0.50
0.25
0.00
***
Free mCherry
Met32 (-met)
F
Fano (normalized)
3.0
2.5
2.0
1.5
1.0
0.5
0.0
***
Free mCherry
Met32 (-met)
G
Met4-GFP
Met32-mCherry
Merged
Sth1-GFP
Met32-mCherry
Merged
H
Met4-Met32
STH1-Met32
Count
40
30
20
10
0
0.0 0.1 0.2 0.3 0.4 0.5 0.6 0.7 0.8 0.9 1.0
GFP-mCherry Correlation Coefficient

A

Protein	FuzDrop
Met4	0.9964
Met32	0.7066
Met31	0.4117
Met28	0.4828
eGFP	0.2134
mCherry	0.2805

B

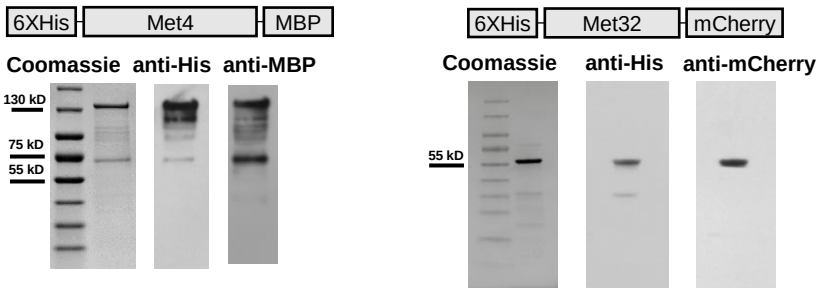

C

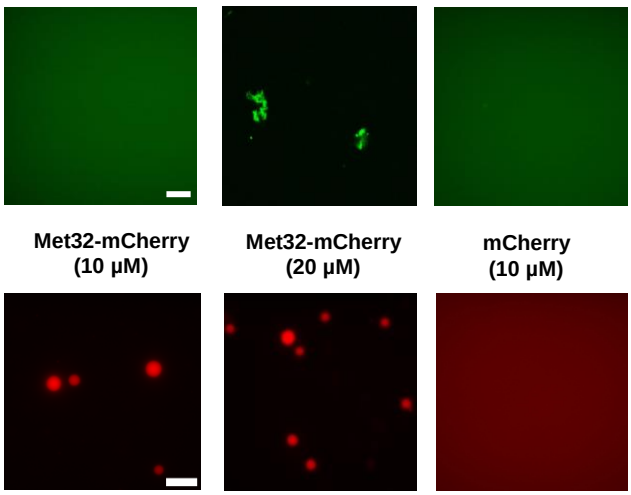

D

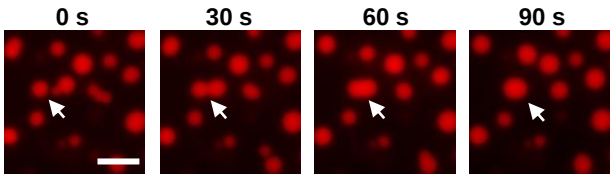

E

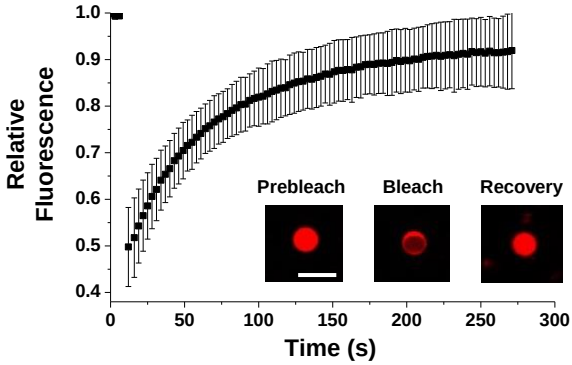

F

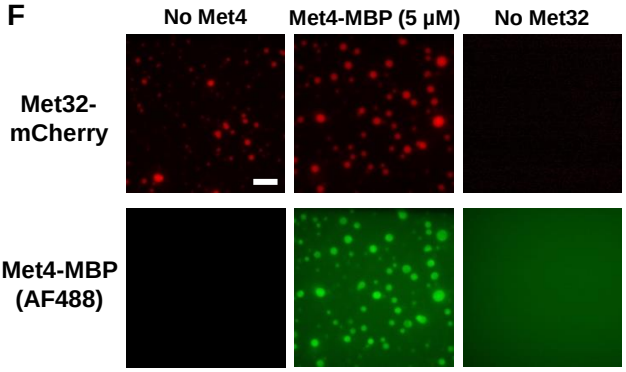

Figure 3

Lee et al.

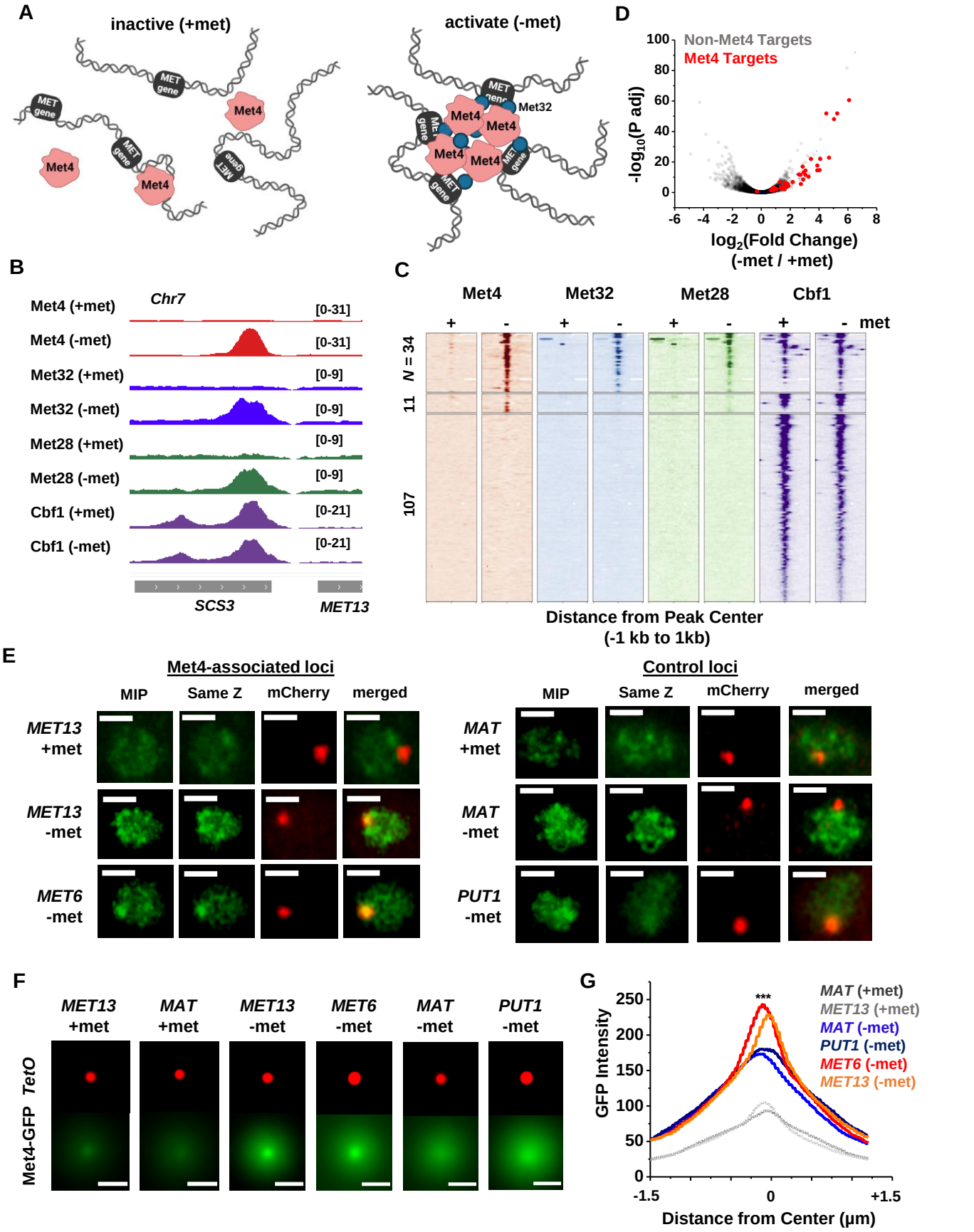

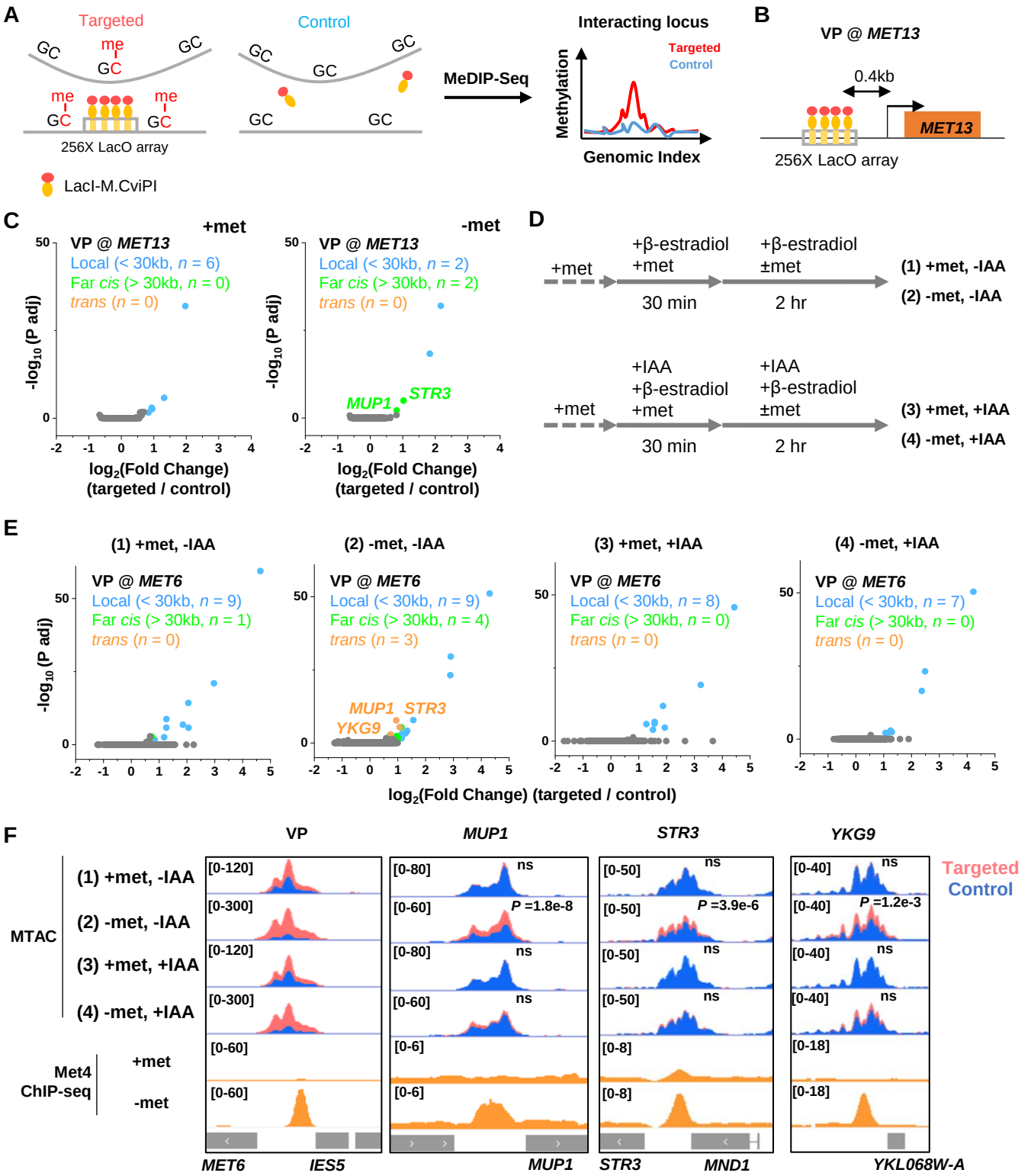
A
Targeted
Control
me
GC
256X LacO array
LacI-M.CviPI
MeDIP-Seq
Interacting locus
Methylation
Genomic Index
B
VP @ MET13
0.4kb
MET13
256X LacO array
C
+met
-met
VP @ MET13
Local (< 30kb, n = 6)
Far cis (> 30kb, n = 0)
trans (n = 0)
Local (< 30kb, n = 2)
Far cis (> 30kb, n = 2)
trans (n = 0)
MUP1
STR3
-log10 (P adj)
log2(Fold Change)
(targeted / control)
D
+met
+β-estradiol
+met
30 min
+β-estradiol
±met
2 hr
(1) +met, -IAA
(2) -met, -IAA
+IAA
+β-estradiol
+met
+IAA
+β-estradiol
±met
(3) +met, +IAA
(4) -met, +IAA
E
(1) +met, -IAA
(2) -met, -IAA
(3) +met, +IAA
(4) -met, +IAA
VP @ MET6
Local (< 30kb, n = 9)
Far cis (> 30kb, n = 1)
trans (n = 0)
Local (< 30kb, n = 9)
Far cis (> 30kb, n = 4)
trans (n = 3)
Local (< 30kb, n = 8)
Far cis (> 30kb, n = 0)
trans (n = 0)
Local (< 30kb, n = 7)
Far cis (> 30kb, n = 0)
trans (n = 0)
MUP1
STR3
YKG9
-log10 (P adj)
log2(Fold Change) (targeted / control)
F
VP
MUP1
STR3
YKG9
MTAC
(1) +met, -IAA
(2) -met, -IAA
(3) +met, +IAA
(4) -met, +IAA
Met4 ChIP-seq
+met
-met
Targeted
Control
[0-120]
[0-300]
[0-60]
[0-80]
[0-6]
[0-50]
[0-8]
[0-40]
[0-18]
ns
P =1.8e-8
P =3.9e-6
P =1.2e-3
MET6
IES5
MUP1
STR3
MND1
YKL068W-A

Figure 5

Lee et al.

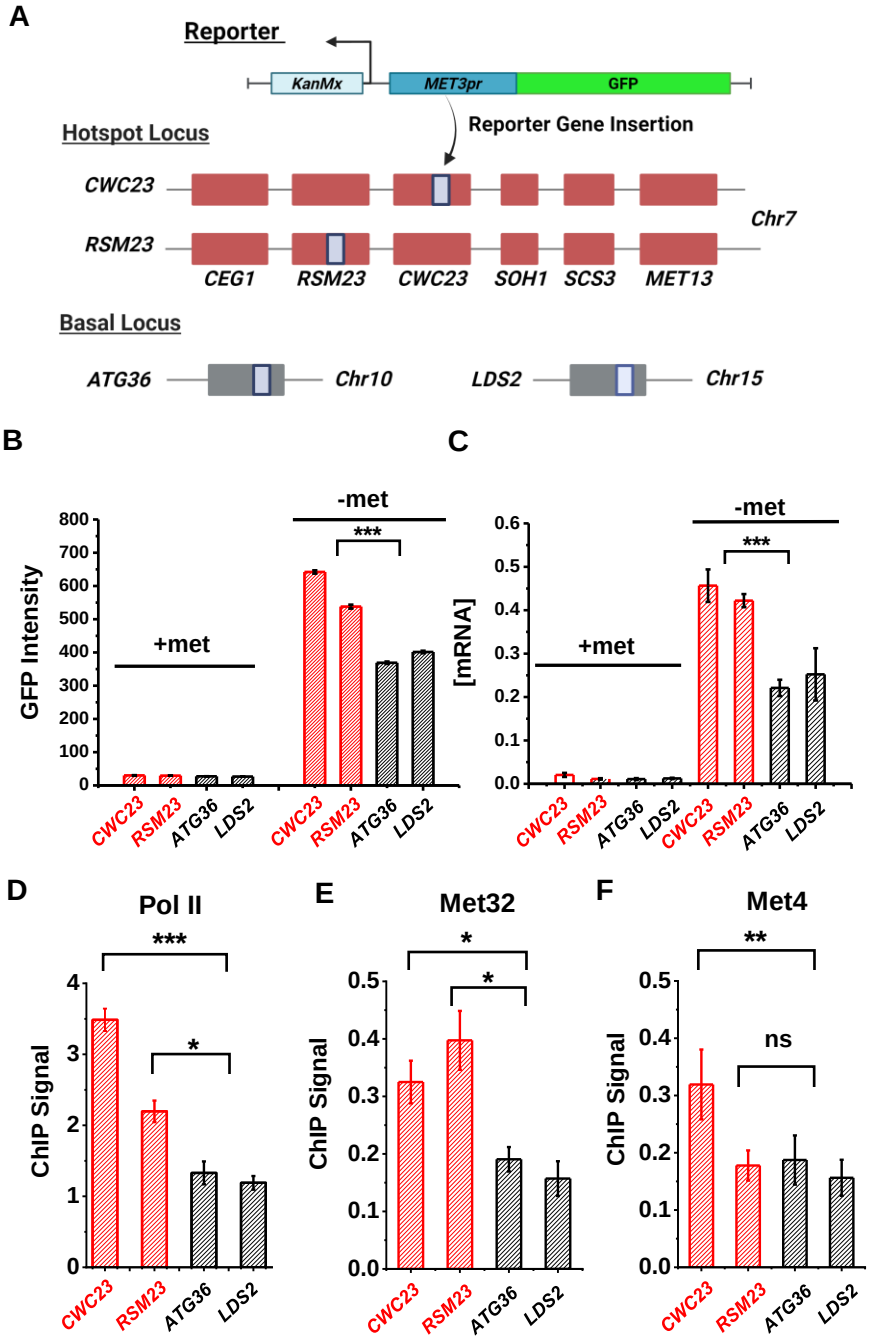

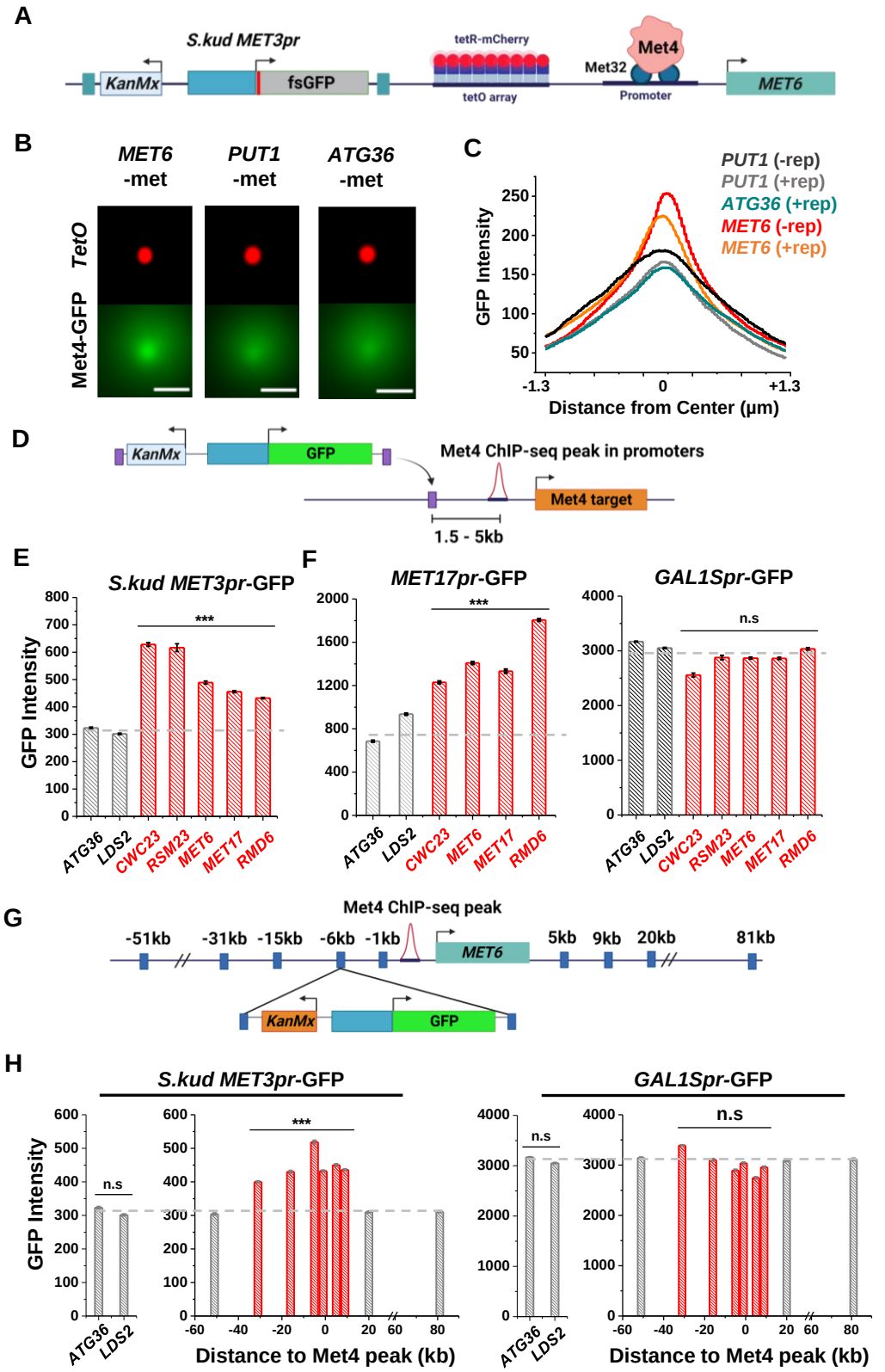
A
S.kud MET3pr
KanMx
fsGFP
tetR-mCherry
tetO array
Met4
Met32
Promoter
MET6
B
MET6 -met
PUT1 -met
ATG36 -met
TetO
Met4-GFP
C
PUT1 (-rep)
PUT1 (+rep)
ATG36 (+rep)
MET6 (-rep)
MET6 (+rep)
GFP Intensity
Distance from Center (μm)
D
KanMx
GFP
Met4 ChIP-seq peak in promoters
Met4 target
1.5 - 5kb
E
S.kud MET3pr-GFP
GFP Intensity
ATG36
LDS2
CWC23
RSM23
MET6
MET17
RMD6
F
MET17pr-GFP
GAL1Spr-GFP
n.s
G
Met4 ChIP-seq peak
-51kb
-31kb
-15kb
-6kb
-1kb
5kb
9kb
20kb
81kb
MET6
KanMx
GFP
H
S.kud MET3pr-GFP
GAL1Spr-GFP
GFP Intensity
Distance to Met4 peak (kb)

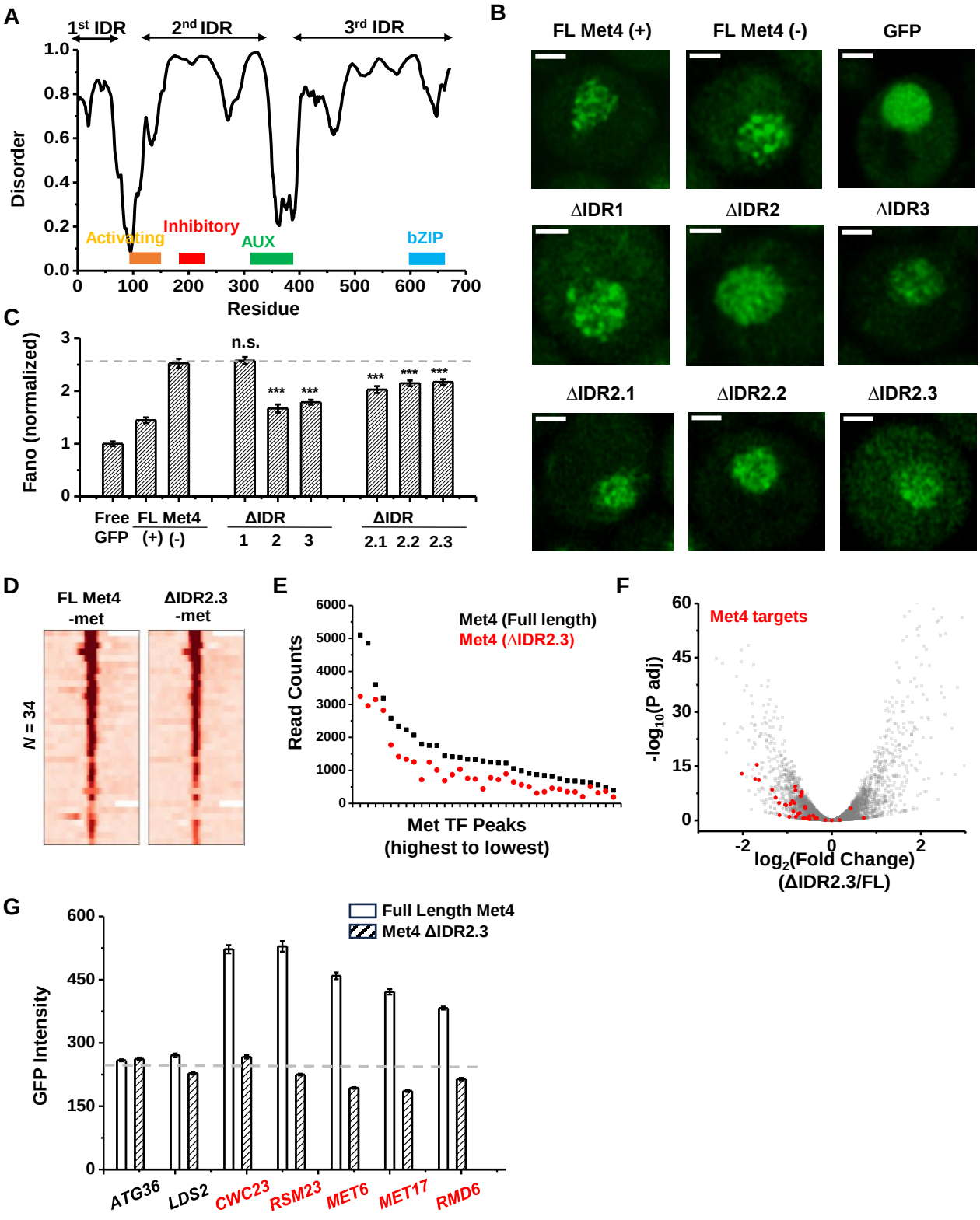
A
1st IDR
2nd IDR
3rd IDR
Disorder
Residue
Activating
Inhibitory
AUX
bZIP
B
FL Met4 (+)
FL Met4 (-)
GFP
ΔIDR1
ΔIDR2
ΔIDR3
ΔIDR2.1
ΔIDR2.2
ΔIDR2.3
C
Fano (normalized)
n.s.
***
Free GFP
FL Met4 (+) (-)
ΔIDR 1 2 3
ΔIDR 2.1 2.2 2.3
D
FL Met4 -met
ΔIDR2.3 -met
N = 34
E
Read Counts
Met4 (Full length)
Met4 (ΔIDR2.3)
Met TF Peaks (highest to lowest)
F
Met4 targets
-log10(P adj)
log2(Fold Change) (ΔIDR2.3/FL)
G
Full Length Met4
Met4 ΔIDR2.3
GFP Intensity
ATG36
LDS2
CWC23
RSM23
MET6
MET17
RMD6